#### **OPEN ACCESS**



# Search for Supernova Progenitor Stars with ZTF and LSST

Nora L. Strotjohann b, Eran O. Ofek b, Avishay Gal-Yam b, Jesper Sollerman b, Ping Chen Graron b, Rarak Zackay b, Nabeel Rehemtulla b, Phillipe Gris Frank J. Masci b, Ben Rusholme b, and Josiah Purdum beratuen of Particle Physics and Astrophysics, Weizmann Institute of Science, 76100 Rehovot, Israel bepartment of Astronomy, The Oskar Klein Center, Stockholm University, AlbaNova, SE-10691 Stockholm, Sweden bepartment of Physics and Astronomy, Northwestern University, 2145 Sheridan Road, Evanston, IL 60208, USA Center for Interdisciplinary Exploration and Research in Astrophysics (CIERA), 1800 Sherman Avenue, Evanston, IL 60201, USA Laboratoire de Physique de Clermont, IN2P3/CNRS, F-63000 Clermont-Ferrand, France PIPAC, California Institute of Technology, 1200 E. California Boulevard, Pasadena, CA 91125, USA Caltech Optical Observatories, California Institute of Technology, Pasadena, CA 91125, USA Received 2023 March 1; revised 2023 October 9; accepted 2023 October 22; published 2023 December 27

#### **Abstract**

The direct detection of core-collapse supernova (SN) progenitor stars is a powerful way of probing the last stages of stellar evolution. However, detections in archival Hubble Space Telescope images are limited to about one detection per year. Here, we explore whether we can increase the detection rate by using data from ground-based wide-field surveys. Due to crowding and atmospheric blurring, progenitor stars can typically not be identified in preexplosion images alone. Instead, we combine many pre-SN and late-time images to search for the disappearance of the progenitor star. As a proof of concept, we implement our search of ZTF data. For a few hundred images, we achieve limiting magnitudes of  $\sim$ 23 mag in the g and r bands. However, no progenitor stars or long-lived outbursts are detected for 29 SNe within  $z \le 0.01$ , and the ZTF limits are typically several magnitudes less constraining than detected progenitors in the literature. Next, we estimate progenitor detection rates for the Legacy Survey of Space and Time (LSST) with the Vera C. Rubin telescope by simulating a population of nearby SNe. The background from bright host galaxies reduces the nominal LSST sensitivity by, on average, 0.4 mag. Over the 10 yr survey, we expect the detection of  $\sim$ 50 red supergiant progenitors and several yellow and blue supergiants. The progenitors of Type Ib and Ic SNe will be detectable if they are brighter than -4.7 or -4.0 mag in the LSST i band, respectively. In addition, we expect the detection of hundreds of pre-SN outbursts depending on their brightness and duration.

*Unified Astronomy Thesaurus concepts:* Core-collapse supernovae (304); Massive stars (732); Red supergiant stars (1375); Sky surveys (1464)

Supporting material: machine-readable tables

#### 1. Introduction

While thousands of core-collapse supernovae (SNe) are discovered and classified every year, <sup>8</sup> detecting their faint progenitor stars is much more challenging. Therefore, we cannot be certain that they are similar to the well-studied stars in the Milky Way or Magellanic clouds.

Direct progenitor star detections so far (see, e.g., Smartt 2015; Van Dyk 2017 for reviews) have established that the progenitors of Type II supernovae (SNe II) are red supergiants (RSGs) and Type IIb supernovae (SNe IIb) have been observed to arise from yellow supergiants (YSGs). Slowly rising, SN 1987A-like SNe II are the explosions of more compact blue supergiants (BSGs), and at least some interacting Type IIn supernovae (SNe IIn) are believed to originate from luminous blue variables (see, e.g., Gal-Yam et al. 2007; Smith 2017). Less is known about the progenitor stars of other, rarer SN types, like Type Ibc or Ibn supernovae (SNe Ibc and SNe Ibn, respectively; see, e.g., Eldridge & Maund 2016; Xiang et al. 2019; Kilpatrick et al. 2021 for potential detections). SN observations indicate that their progenitors are partially or completely stripped, massive stars.

Original content from this work may be used under the terms of the Creative Commons Attribution 4.0 licence. Any further distribution of this work must maintain attribution to the author(s) and the title of the work, journal citation and DOI.

The stripping presumably requires either strong winds or a binary partner.

The Hubble Space Telescope (HST) has been very successful at detecting progenitor stars. However, detections are only attained at a rate of about one progenitor per year (see, e.g., Davies & Beasor 2018), such that increasing the sample size substantially would require decades of observations. Archival HST observations are available for about 25% of the closest SNe (Smartt 2015), and identifying a progenitor star securely requires both precise astrometry and additional late-time HST observations to verify that the progenitor candidate has indeed vanished (see, e.g., Crockett et al. 2011; Maund et al. 2014, 2015b; Van Dyk et al. 2023). This confirmation is crucial as some of the brightest progenitor candidates have turned out to be stellar clusters rather than single stars (e.g., Maund & Smartt 2009; Maund et al. 2015b; Van Dyk et al. 2023).

Smartt (2015; and earlier Smartt et al. 2009) compiled a sample of detected progenitor stars and compared their inferred masses to predictions by stellar models. Smartt (2015) find that all 26 RSG mass estimates and upper limits are fainter than  $\log_{10}(L/L_{\odot}) \leq 5.2$ , corresponding to a bolometric magnitude of -8.2 mag. Based on stellar evolution models, they conclude that all progenitors had initial masses of  $<18~M_{\odot}$ , while they would expect that 30% of the progenitors are more massive. This discrepancy, pointed out earlier by Li et al. (2006) and Kochanek et al. (2008), was coined the RSG problem, and Smartt (2015) suggests that the most massive stars collapse into

see, e.g., https://www.wis-tns.org/stats-maps.

black holes without producing a bright SN. Such failed SNe are also predicted by studies that simulate stellar cores (see, e.g., Patton & Sukhbold 2020 for a recent result), and a few candidates have been reported (Reynolds et al. 2015; Basinger et al. 2021; Neustadt et al. 2021).

However, the lack of bright SN progenitors was diagnosed based on sparse observations. SN progenitor stars are usually only detected in one or a few HST observations, often in a single band. Thus, the star's surface temperature and bolometric luminosity cannot be estimated reliably (see, e.g., Smartt 2015; Davies & Beasor 2018). Other uncertainties are induced by host extinction, circumstellar dust (e.g., Kochanek et al. 2012), uncertain SN distances, and the small number of progenitor detections (Davies & Beasor 2018). Consequently, it is under debate whether the RSG problem is significant (e.g., Davies & Beasor 2018, 2020; Kochanek 2020; Rodríguez2022).

An additional complication is that the impending core collapse might trigger mass-loss events that change the progenitor's temperature and luminosity; violent stellar eruptions are common prior to SNe IIn (Ofek et al. 2014; Strotjohann et al. 2021), and similar, but fainter, outbursts were also detected prior to SNe II (Jacobson-Galán et al. 2022a), SNe Ibn (Pastorello et al. 2007; Strotjohann et al. 2021), broad-lined SNe Ic (Ho et al. 2019), and potentially SNe IIb (Strotjohann et al. 2015). In addition, Margutti et al. (2017) and Sollerman et al. (2020) observed late-time interaction for three SNe Ib, which indicates a major mass-loss event shortly before each SN explosion. The spectra of young SNe indicate that a large fraction of them explode within a confined shell of circumstellar material (Khazov et al. 2016; Bruch et al. 2021, 2023), which points to increased mass loss in the last years before the core collapse. Outbursts that inflate stellar envelopes have also been proposed to explain the fast rise times and hot temperatures of young SNe (Förster et al. 2018; Morozova et al. 2020). Mass-loss events can boost the progenitor luminosity, e.g., due to interaction with the ejected material. However, absorption or inflated envelopes can also redden the stellar spectrum and reduce the progenitor luminosity (Davies et al. 2022). Pre-SN outbursts can hence cause dimming or brightening in a single band.

Most of the described challenges could be mitigated by a larger sample of SN progenitors detected in several bands and epochs. Therefore, we explore here whether ground-based, large-field-of-view surveys are sensitive enough to detect the closest SN progenitor stars. We consider two surveys: the Zwicky Transient Facility (ZTF; Bellm et al. 2019; Graham et al. 2019; Dekany et al. 2020) that has been running since 2018 and the planned, more sensitive Legacy Survey of Space and Time (LSST; Ivezić et al. 2019). Due to blurring by the atmosphere, stars in nearby galaxies are blended with each other, such that pre-SN data alone are usually not sufficient to pinpoint the progenitor. The angular resolution of ZTF observations is typically limited by the median seeing of 2'', while a median seeing of 0."65 is expected for the LSST site (Ivezić et al. 2019). In contrast, the HST Wide Field Camera 3 has a much smaller point-spread function (PSF) width of  $\sim$ 0."1 in the infrared (Dressel & Marinelli 2023). To detect the progenitor despite the lower resolution, we combine many images before the SN and after it has faded and search for a flux difference between these two time windows. The search does not require dedicated observations and can be done for any position monitored by a survey.

Ground-based, wide-field surveys have so far detected a few progenitor stars: the bright YSG progenitor of SN 2011dh was detected by the Palomar Transient Factory (PTF; Strotjohann et al. 2015), the Large Binary Telescope (Szczygiełet al. 2012), and the Nordic Optical Telescope (Ergon et al. 2015). Combining hundreds of PTF images before and after the SN confirmed that the progenitor of SN 2011dh had indeed disappeared. The same search was sensitive enough to disfavor a progenitor candidate for another SN IIb, SN 2012P, as it was still present after the SN had faded. In a more recent search, we detected the progenitor star of the IIn SN 2019cmy at a seemingly constant luminosity of -14 mag in the ZTF g and rbands in the last year before the SN explosion (Strotjohann et al. 2021). However, the star is fainter in earlier PTF observations (M. Soumagnac et al. 2023, in preparation); we hence likely observe a long-lasting outburst rather than a quiescent progenitor star. Progenitors in their quiescent state are many magnitudes fainter and the low temperatures of RSGs make their detection in visible bands even more challenging.

In Section 2, we conduct a progenitor search for ZTF data as a proof of concept and compare the ZTF results to earlier progenitor detections. In Section 3, we quantify how sensitive LSST will be to progenitor stars and pre-SN outbursts, and we conclude in Section 4.

# 2. Search for Progenitor Stars in ZTF Data

As a test, we implement our progenitor search for the closest SNe in ZTF data. Section 2.1 describes the sample selection, and Section 2.2 explains the details of the search. Results are presented in Section 2.3, and we compare to progenitor detections in the literature in Section 2.4. Finally, in Section 2.5 we quantify whether the search is as sensitive as expected. Appendix A provides more details on the photometric pipeline and error sources, and we verify the sensitivity of the search by injecting faint, artificial sources into the images and quantifying their recoverability.

## 2.1. Sample Selection

Our ZTF search is based on SNe detected by the Bright Transient Survey (BTS; Fremling et al. 2020; Perley et al. 2020). The ZTF pipeline (Masci et al. 2019) uses the ZOGY image subtraction algorithm (Zackay et al. 2016) and yields  $>10^6$  potential detections per night (Patterson et al. 2019), but quality cuts reduce the number of SN candidates to  $\sim$ 50 per night (Perley et al. 2020). An on-duty astronomer searches the remaining candidates for genuine, SN-like transients that surpass the brightness threshold of 18.5 mag in the g or r band. The selected objects are classified with the SEDM spectrograph on the P60 telescope (Blagorodnova et al. 2018; Rigault et al. 2019; Kim et al. 2022), and discoveries are reported to the Transient Name Server and the BTS sample explorer. For our search, we select 60 SNe that exploded between 2018 and 2021 within  $z \leq 0.01$  or 45 Mpc.

The luminosity distances of nearby SNe are rather uncertain, and, if available, we use the more precise host galaxy redshift instead of the SN redshift. We here adopt the preferred redshift from the NASA/IPAC Extragalactic Database<sup>11</sup> and convert it to the infall-corrected distance. For SN 2018ebt, we measure a

https://www.wis-tns.org/

https://sites.astro.caltech.edu/ztf/bts/explorer.php

<sup>11</sup> https://ned.ipac.caltech.edu/

host redshift of z = 0.0095 from galaxy lines in a late-time spectrum. After refining the redshifts, we are left with 55 SNe within 45 Mpc.

Next, we download IPAC difference images (IRSA 2022)<sup>12</sup> and calculate forced-photometry light curves for the remaining SNe as described in Appendix A.1. We inspect the light curves visually and, if necessary, correct the approximate explosion date,  $t_0$ , to ensure that the selected pre-SN observations do not contain any SN light. Conservatively, we only combine observations obtained more than 10 days before  $t_0$  to calculate the preexplosion flux. IPAC produces a single ZTF reference image for each combination of ZTF field, filter, CCD number, and CCD quadrant (Masci et al. 2019). In the following, we call each unique combination of these parameters a field and only compare difference images in the same field, i.e., that were produced with the same reference image. We require at least 15 pre-SN observations in the same field and discard three out of 55 SNe because they do not have enough pre-SN observations. We also use the selected pre-SN observations to do a baseline correction to ensure that the pre-SN light curve corresponds to zero flux and we scale up the error bars if they are too small to account for the observed scatter (details are given in Appendix A.1).

The expected sensitivity of our search is  $\sim$ 23 mag, and we extrapolate the late-time SN light curves to determine when they have faded below this threshold. To gain sensitivity to the faint late-time fluxes, we combine the g- and r-band fluxes in 7 day bins as described in Appendix A.1. To avoid marginal detections, we select the second to last r-band detection and extrapolate it with a slope of 1 mag per 100 days, the decay rate of <sup>56</sup>Co. Two SNe, SN 2018ivc and SN 2018ebt, have no, or few, r-band observations that pass our quality cuts (described in Appendix A.1) and we extrapolate their g-band light curves instead but increase the flux by 0.5 mag as SNe are typically brighter in the r band at this time. We acknowledge that some SNe might fade more slowly at late times, e.g., due to the latetime interaction (Sollerman et al. 2020; Weil et al. 2020) or light echoes (Maund 2019) which might yield false nondetections. The best way to mitigate this is by inspecting the latetime light curves carefully, and using several different time windows to calculate the late-time flux.

Of the 52 nearby SNe with pre-SN observations 29 have already faded below magnitude 23 and Table 1 lists their properties. Unbinned forced-photometry light curves are provided in Table 2. Figure 1 shows the forced-photometry light curves in 7 day bins. The orange shaded regions in the figures indicate the time when the SN is likely brighter than 23rd magnitude and we use the observations before and after to calculate the pre-SN and late-time fluxes, respectively. Our sample includes 18 SNe II or IIP. SN 2018hna (Singh et al. 2019) has an SN 1987A-like light curve and its progenitor is presumably a more compact BSG. The remaining 11 SNe originate from, at least partially, stripped progenitor stars: two are classified as SNe IIb, five are SNe Ib, three are SNe Ic, and one is a broad-lined SN Ic. The two closest SNe Ib in our sample belong to the subclass of low-energy, calcium-rich SNe.

# 2.2. The Progenitor Search

The low spatial resolution of ground-based surveys like ZTF does not allow us to reliably identify the progenitor star in pre-

SN images alone as each pixel contains the light from many stars. But the vanishing of the progenitor star reduces the flux at the SN position and we search for this flux residual by comparing pre-SN images to observations taken after the SN has faded.

Table 3 lists all fields with at least 20 observations before and after the SNe, and their light curves are shown in Figure 1. For each field, we calculate the mean flux, weighted according to the flux error bars, before and after the SN. We only compare observations that have the same reference image. We estimate the flux error with the bootstrap method (Efron 1982) by resampling both the pre-SN and late-time fluxes while allowing for repetitions. For each randomized light curve we calculate the weighted mean flux before and after the SN and the difference between the two. The standard deviation of the resulting distribution of residuals is used as the error on the flux residual. The advantage of the bootstrap method is that the results are valid even if the flux errors are inaccurate or not Gaussian. By using the weighted mean, we assume, however, that the relative size of the error bars is correct.

Combining hundreds of observations reduces statistical fluctuations, therefore, our search might be limited by additional errors and systematics, such as residuals due to bright host galaxies, shallow reference images, a bias mismatch, or errors on the PSF. In Appendix A.2, we quantify the impact of these error sources empirically: we select 20 positions in the same images that have host fluxes similar to the SN position and perform a progenitor search at each position. For appropriately large error bars the standard deviation of these flux residuals should be close to one. If it is larger, the errors are likely underestimated, and we scale them up, i.e., we scale down the significance of the progenitor detection (see Appendix A.2 for details). The resulting scaling factors are given in the seventh column of Table 3. A few fields have scaling factors as large as two, sometimes due to a bright host, while in other cases, we cannot pinpoint what limits the sensitivity. However, most scaling factors are close to one, indicating that the sensitivity is determined by well-understood statistical fluctuations and that additional ZTF observations might improve the depth of the search.

# 2.3. Results

All flux residuals, their errors, and their significances are listed in Table 3. Our search yields a single  $5\sigma$  detection: when combining the g-band observations of SN 2020cxd (Yang et al. 2021; Kozyreva et al. 2022; Valerin et al. 2022) we measure a flux residual of  $22.7 \pm 0.2$  mag (shown as a green data point in Figure 2). We inspect the 30 day binned light curve of SN 2020cxd, and Figure A1 shows that both the g- and r-band fluxes are fading over the 4 yr during which ZTF monitored the position. The trend seems to continue after the SN explosion, implying that it is either due to an unrelated background source or due to long-term changes in the calibration. We did not observe similar variability for any of the 20 background positions in the same galaxy, so it is likely a local effect. A single ZTF pixel covers 1."012 in the sky, corresponding to 110 kpc in the host galaxy NGC 6395. Therefore, it is possible that the fading originates from an unrelated source. We thus conclude that unrelated variable sources and progenitor outbursts are a potential contamination for our search. We do not find any genuine detections and the ZTF limiting magnitudes of our progenitor search are shown in Figure 2.

<sup>&</sup>lt;sup>12</sup> Including data until 2022 August.

Table 1 Nearby BTS SNe

IAU Name	ZTFID	R.A. (deg)	Decl. (deg)	Type	(JD)	t <sub>23</sub> (days)	Host	Distance (Mpc)	Progenitor Det.
SN 2020jfo	ZTF 20aaynrrh	185.460355	4.481697	SN II	2,458,974.7	569	M 61	14.7	$25.47 \pm 0.07$ (F814W) (a)
SN 2020fqv	ZTF 20aatzhhl	189.138575	11.231653	SN II	2,458,937.8	612	NGC 4568	14.9	>24.8 (F606W) (b)
SN 2018imf	ZTF 18acqsqrg	190.672493	13.265236	SN II	2,458,438.0	617	NGC 4639	15.0	, , , , ,
SN 2019ehk	ZTF 19aatesgp	185.733956	15.826127	SN Ib	2,458,602.7	517	NGC 4321	15.1	>28.7 (F555W) (c)
	Ci			(Ca rich)					
SN 2020oi	ZTF 20aaelulu	185.728855	15.823611	SN Ic	2,458,855.9	570	NGC 4321	15.1	bright cluster (d)
SN 2021gno	ZTF 21aaqhhfu	183.042900	13.249178	SN Ib (Ca	2,459,293.7	358	NGC 4165	15.1	-
				rich) (e)					
SN 2018ivc	ZTF 18acrcogn	40.671990	-0.008900	SN II	2,458,447.9	565	NGC 1068	16.4	>25.4 (F606W) (f)
SN 2018hna	ZTF 18acbwaxk	186.550338	58.314126	SN II	2,458,420.9	751	UGC 07534	16.5	
				(BSG) (g)					
SN 2020cxd	ZTF 20aapchqy	261.621952	71.094062	SN II	2,458,898.0	333	NGC 6395	23.6	
SN 2020dpw	ZTF 20aauhbvu	309.293939	66.102971	SN II	2,458,936.0	724	NGC 6951	26.1	
SN 2020hvp	ZTF 20aavzffg	245.439146	-2.289270	SN Ib	2,458,962.9	561	NGC 6118	25.2	
SN 2020mjm	ZTF 20abeohfn	217.372229	-0.021626	SN II	2,459,012.2	620	UGC 09299	28.3	
SN 2020mmz	ZTF 20abevbxv	140.298238	64.253968	SN II	2,459,012.7	563	NGC 2814	28.9	
SN 2019yvr	ZTF 20aabqkxs	191.283891	-0.459114	SN Ib	2,458,846.0	772	NGC 4666	29.4	$24.9 \pm 0.02$
									(F635W) (h)
SN 2020vg	ZTF 20aafclxb	177.226830	-4.681626	SN II	2,458,860.0	536	NGC 3915	29.4	
SN 2020abhs	ZTF 20actodrq	193.739146	-13.541537	SN II	2,459,174.0	359	•••	31.2 (i)	
SN 2019spk	ZTF 19acecluy	150.726656	-6.207211	SN II	2,458,756.0	454	PGC 166103	32.6	
SN 2021bug	ZTF 21aagydmn	188.594858	2.317296	SN II	2,459,249.9	305	NGC 4533	32.6	
SN 2021bhd	ZTF 21aagbpvf	207.061475	68.089699	SN Ib	2,459,230.9	349	UGC 08737	33.2	
SN 2019yz	ZTF 19aadttht	235.488760	0.710949	SN Ic	2,458,501.0	583	UGC 09977	34.6	
SN 2020fsb	ZTF 20aaunfpj	234.765872	-25.974543	SN II	2,458,936.9	692	ESO 515-G004	34.7	
SN 2019bzd	ZTF 19aamwhat	221.883498	-19.766047	SN II	2,458,560.8	619	ESO 580-029	39.9	
SN 2019pjs	ZTF 19abwztsb	271.168089	21.634511	SN II	2,458,730.7	610	UGC 11105	40.1	
SN 2019enr	ZTF 19aatwvft	143.698711	10.286955	SN II	2,458,608.2	503	NGC 2919	40.6	
SN 2018ebt	ZTF 18abjrbza	310.479145	64.214621	SN Ic	2,458,315.9	596	•••	42.4	
SN 2018gjx	ZTF 18abwkrbl	34.064926	28.591298	SN IIb	2,458,374.9	378	NGC 0865	43.2	
SN 2019aai	ZTF 19aadtqcd	248.086436	19.840120	SN II	2,458,502.0	311	NGC 6181	43.2	
SN 2019lkx	ZTF 19abgiwkt	55.262133	34.652071	SN II	2,458,677.9	645	•••	44.6 (i)	
SN 2020tkx	ZTF 20abzoeiw	280.037525	34.116527	SN Ic-BL	2,459,108.8	446	•••	44.6 (i)	

**Notes.** All SNe with  $\ge 20$  data points before and after the SN in the same field. Data obtained more than 10 days before  $t_0$  are used to measure the preexplosion flux. At  $t_{23}$  the SN has likely faded to 23rd magnitude in the r band and we combine later observations to measure the late-time flux.

**References.** (a) Sollerman et al. (2021); (b) Tinyanont et al. (2022); (c) Jacobson-Galán et al. (2020); (d) Gagliano et al. (2022); (e) Jacobson-Galán et al. (2022b); (f) Bostroem et al. (2020); (g) Singh et al. (2019); (h) Kilpatrick et al. (2021), likely a binary system; Sun et al. (2022); (i) no host galaxy redshift available. We use the less precise SN redshift.

(This table is available in machine-readable form.)

 Table 2

 Unbinned ZTF Forced-photometry Light Curves for 29 Nearby SNe

SN Name	JD (2,450,000+)	FCQFID	Flux (10 <sup>-9</sup> mgy)	Flux Error (10 <sup>-9</sup> mgy)
SN 2020jfo	8199.80343	4730622	-5.3	3.6
SN 2020jfo	8204.80090	4730621	1.2	2.7
SN 2020jfo	8204.81700	4730621	-1.2	2.5
SN 2020jfo	8210.80147	4730621	-8.1	4.7
SN 2020jfo	8214.73870	4730622	4.5	3.4

**Notes.** We removed all data points that do not pass our quality cuts, applied a baseline correction, and rescaled the flux uncertainties based on the observed scatter of the pre-SN observations (see Appendix A). The third column encodes the ZTF field (first three to five digits), CCD ID (fourth and third last digits), quadrant ID (second to last digit), and filter (last digit) of the ZTF observations. Fluxes are given in maggies. The full table contains 29,305 observations and is published online.

(This table is available in its entirety in machine-readable form.)

#### 2.4. SN Progenitor Detections in the Literature

So far, progenitor searches in HST images have been published for six of the SNe in the ZTF sample (see Table 1). The closest object, SN 2020jfo, has a rather faint progenitor star with  $25.47 \pm 0.07$  or -5.35 mag in the F814W band (Sollerman et al. 2021). Moreover, the detection of an SN Ib progenitor was reported for SN 2019yvr (Kilpatrick et al. 2021) and the colors imply an F-type spectrum. Late-time observations will reveal, whether it is a single star, binary system, or dense stellar cluster (Sun et al. 2022). The progenitors of SN 2018ivc, SN 2019ehk, and SN 2020fqv remain undetected (see Bostroem et al. 2022); Jacobson-Galán et al. 2020; Tinyanont et al. 2022), while a bright stellar cluster was detected at the position of SN 2020oi (Gagliano et al. 2022).

Samples of progenitor searches have, for example, been presented by Smartt (2015) and Van Dyk (2017; for all SN types) and Davies & Beasor (2018; for RSG progenitors). We update the Davies & Beasor (2018) and Davies & Beasor

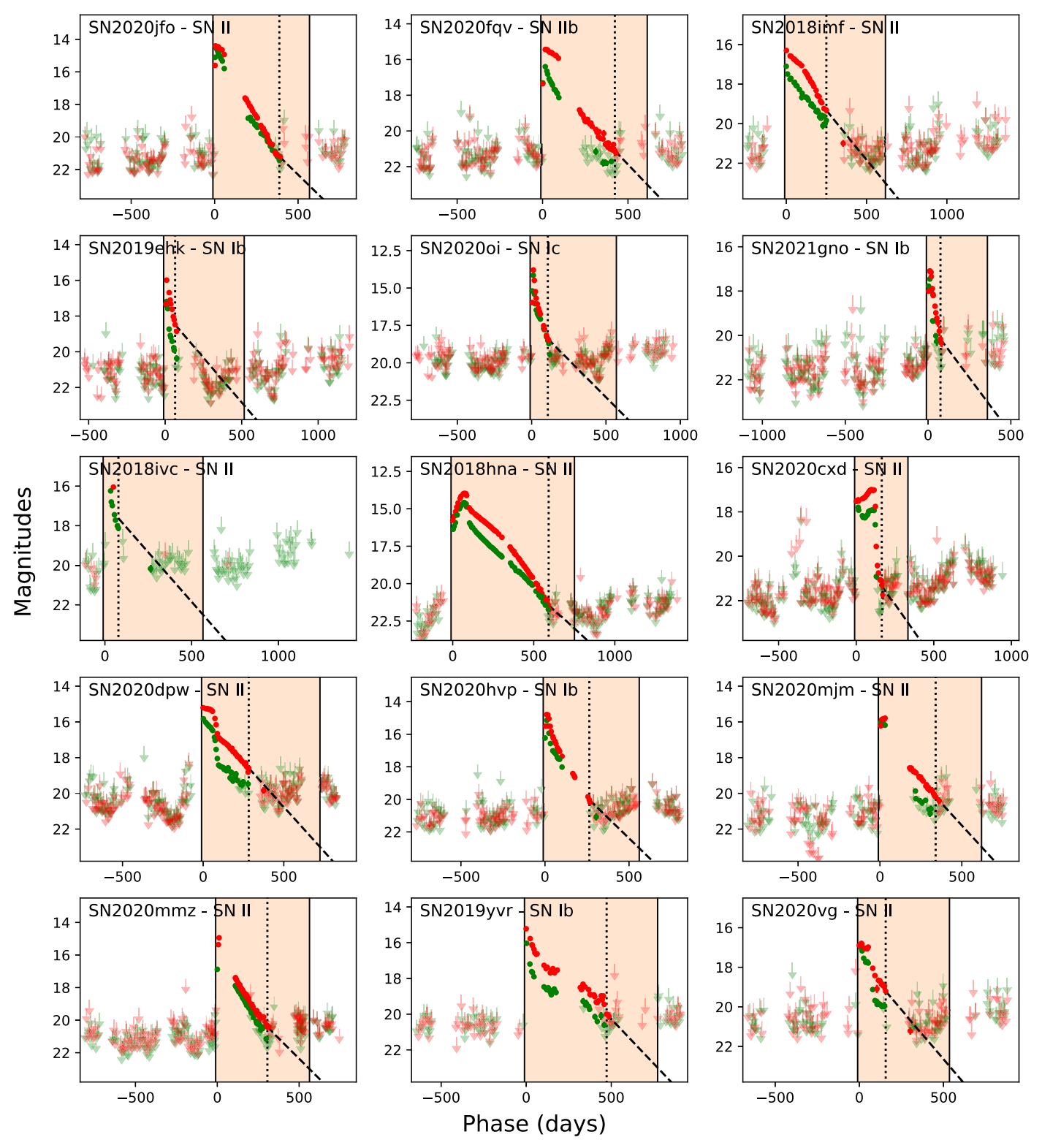


**Figure 1.** Light curves in week-long bins for 29 nearby SNe with enough observations before and after the SN. To determine whether the SN is still present at late times, we identify the second to last  $5\sigma$  detection in the r band and extrapolate the light curve with a slope of 1 mag per 100 days (shown as a dashed line). SN 2018ivc and SN 2018ebt do not have enough r-band observations, so we extrapolate their g-band light curves, but shift the curves by 0.5 mag, as most SNe are brighter in the r band at this time. The orange shaded area marks the time when the SN is likely brighter than 23 mag in the ZTF r band and we combine observations before and after the SN, respectively, to measure both the early- and late-time flux at the SN position.

(2020) sample by adding more recent detections and limits and we discard three progenitor candidates that are not detected securely (SN 2009hd, SN 2009kr, and SN 2009md; Elias-Rosa

et al. 2011; Maund et al. 2015b). We also compile a sample of detected, non-RSG progenitors in Table 8. Host extinction estimates are taken from the literature and, like the SN distance

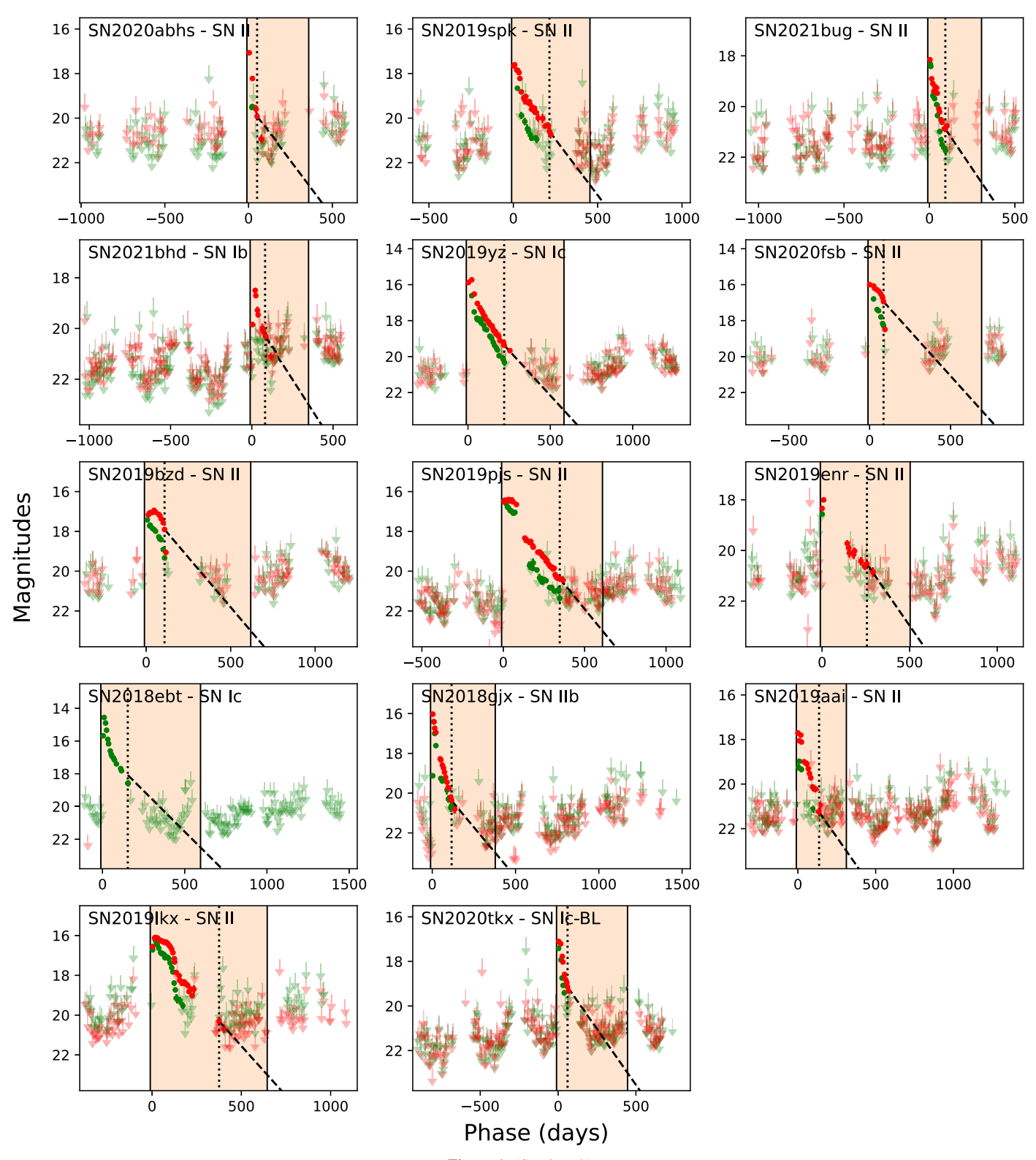


Figure 1. (Continued.)

estimates, they are often uncertain (see, e.g., Maund 2017). We do not consider dust which might reduce the impact of extinction in some bands (Kochanek et al. 2012).

We aim to compare the ZTF limits to direct observations and not to derived quantities. Therefore, we look up the original progenitor observations in individual bands and convert them to ZTF r-band AB magnitudes as described in Appendix B. If

the progenitor is detected in several bands, we pick the band that is closest to the ZTF r band. We use filter profiles from the pyphot library <sup>13</sup> if available or from the database of the Spanish Virtual Observatory <sup>14</sup> and adopt the spectral shapes of giant or

https://mfouesneau.github.io/pyphot/

<sup>14</sup> https://svo.cab.inta-csic.es

Table 3
Measured Flux Residuals

IAU Name	Band	FCQFID	$n_{ m early}$	$n_{\mathrm{late}}$	Host Flux (10 <sup>-10</sup> mgy arcsec <sup>-2</sup> )	Scaling	Flux (10 <sup>-10</sup> mgy)	Sig.	Limit mag (mag)	Abs. Limit mag (mag)
SN 2020jfo	g	4730621	149	65	$22.2 \pm 0.6$	1.8	$-0.4 \pm 2.7$	-0.2	22.2	-8.6
	r	4730622	191	76	$33.6 \pm 0.8$	1.5	$-0.4 \pm 2.2$	-0.2	22.4	-8.4
SN 2020fqv	g	5250521	168	109	$39.6 \pm 0.9$	1.0	$-0.1 \pm 1.1$	-0.1	23.1	-7.8
CN 2010; C	r	5250522	203	120	$80.4 \pm 2.0$	1.6	$3.6 \pm 2.5$	1.4	22.3	-8.6
SN 2018imf	g	5261221	21	94	$4.7 \pm 0.5$	1.8	$-3.2 \pm 3.2$	-1.0	22.0	-8.9
CNI 2021	r	5261222	29	166	$6.1 \pm 0.6$	1.0	$-1.0 \pm 1.8$	-0.6	22.6	-8.3
SN 2021gno	g	5240911 5240912	200 242	22 23	$3.0 \pm 0.5  5.5 \pm 0.7$	1.2 1.1	$-0.7 \pm 2.5$ $-1.1 \pm 2.5$	-0.3 $-0.4$	22.3 22.3	-8.6 $-8.6$
SN 2019ehk	r	5760331	108	145	$30.0 \pm 0.7$	1.1	$-1.1 \pm 2.3$ $-2.1 \pm 1.5$	-0.4 $-1.4$	22.8	-8.1
511 201 )Clik	$\frac{g}{r}$	5760331	148	218	$63.1 \pm 2.0$	1.2	$-2.7 \pm 1.3$ $-0.7 \pm 1.7$	-0.4	22.7	-8.2
SN 2020oi	r	5760332	189	97	$560.4 \pm 13.9$	1.0	$3.0 \pm 1.6$	1.8	22.7	-8.2
SN 2018ivc	g	4021631	46	143	$298.9 \pm 19.3$	1.9	$1.5 \pm 3.0$	0.5	22.1	-9.0
SN 2018hna	g	7891311	116	146	$1.4 \pm 0.5$	1.0	$-3.0 \pm 1.3$	-2.2	22.9	-8.1
51 · 20 10 iiiii	g	7901611	126	101	$1.2 \pm 0.5$	1.2	$-0.1 \pm 1.9$	-0.1	22.6	-8.5
	g	8190141	101	157	$1.4 \pm 0.5$	1.1	$-0.3 \pm 1.3$	-0.2	23.0	-8.1
	g	8200431	128	113	$1.4 \pm 0.4$	1.6	$0.2 \pm 2.2$	0.1	22.4	-8.7
	r	7891312	123	176	$1.8 \pm 0.6$	1.7	$-11.1 \pm 3.1$	-3.6	22.0	-9.0
	r	7901612	121	156	$1.5 \pm 0.4$	1.2	$-2.4 \pm 1.4$	-1.8	22.9	-8.2
	r	8190142	88	167	$1.5 \pm 0.6$	1.1	$0.3 \pm 1.5$	0.2	22.8	-8.3
	r	8200432	115	142	$1.8 \pm 0.5$	1.2	$-1.2 \pm 1.7$	-0.7	22.6	-8.4
SN 2020cxd	g	8481121	564	232	$18.0\pm1.6$	1.1	$8.1 \pm 1.5$	5.3	22.8	-9.1
	r	8481122	478	234	$27.1 \pm 1.8$	1.0	$0.2 \pm 0.7$	0.3	23.6	-8.3
SN 2020dpw	g	8510431	262	24	$14.4\pm0.5$	1.0	$-0.4 \pm 4.7$	-0.1	21.6	-10.5
	r	8510432	266	33	$42.6 \pm 1.0$	1.0	$-2.6\pm4.3$	-0.6	21.7	-10.4
SN 2020mjm	g	4271631	130	33	$0.2 \pm 0.3$	1.2	$-0.7 \pm 1.8$	-0.4	22.6	-9.7
	r	4271632	341	36	$0.2 \pm 0.4$	1.0	$-2.7 \pm 2.0$	-1.3	22.5	-9.8
SN 2020mmz	g	8161431	290	39	$48.4 \pm 2.1$	1.0	$-2.3 \pm 2.1$	-1.1	22.4	-9.9
	r	8161432	316	58	$79.9 \pm 1.5$	1.2	$-0.6 \pm 1.9$	-0.3	22.6	-9.7
SN 2020hvp	g	4300941	66	30	$10.1 \pm 0.7$	1.0	$-7.5 \pm 3.9$	-1.9	21.8	-10.5
	g	4311231	67	31	$9.4 \pm 0.5$	1.2	$-1.9 \pm 4.1$	-0.5	21.7	-10.6
	r	4300942	107	33	$19.9 \pm 0.6$	1.4	$-1.4 \pm 4.1$	-0.3	21.7	-10.6
CN 2010	r	4311232	119	35	$18.9 \pm 0.9$	1.5	$0.1 \pm 4.0$	0.0	21.7	-10.6
SN 2019yvr	g	4231531	43	29	$83.8 \pm 1.6$	1.3	$-3.7 \pm 3.2$	-1.2	22.0	-10.3
CNI 2020-1-1-	r	4231532	79 40	22	$160.4 \pm 3.4$	1.0	$-0.4 \pm 2.7$	-0.1	22.2	-10.2
SN 2020abhs	g	3211411 3720441	49 66	19 21	$9.2 \pm 0.7 \ 8.5 \pm 0.9$	1.1 1.3	$-1.5 \pm 3.3$ $-6.7 \pm 4.3$	$-0.4 \\ -1.6$	21.9 21.7	-10.5 $-10.8$
	$\frac{g}{r}$	3211412	50	31	$10.5 \pm 0.9$	1.5	$-0.7 \pm 4.5$ $0.9 \pm 4.5$	0.2	21.7	-10.8
SN 2019spk		3661611	45	58	$0.6 \pm 0.3$	1.1	$0.9 \pm 4.3$ $2.4 \pm 3.1$	0.2	22.0	-10.5
514 2017 эрк	g g	4170241	48	98	$0.6 \pm 0.3$ $0.6 \pm 0.2$	1.4	$-0.7 \pm 2.1$	-0.3	22.4	-10.3 $-10.1$
	s r	3661612	45	54	$0.6 \pm 0.2$ $0.6 \pm 0.6$	1.3	$4.0 \pm 3.3$	1.2	21.9	-10.1 $-10.6$
	r	4170242	55	126	$0.9 \pm 0.5$	1.3	$-1.3 \pm 2.8$	-0.5	22.1	-10.4
SN 2021bug	g	4730111	171	69	$8.4 \pm 0.5$	1.2	$2.3 \pm 1.7$	1.4	22.7	-9.9
	r	4730112	228	75	$13.3 \pm 0.6$	1.1	$-2.6 \pm 1.9$	-1.4	22.6	-10.0
SN 2021bhd	g	8450841	555	42	$20.9 \pm 0.7$	1.1	$-1.3 \pm 1.4$	-1.0	22.9	-9.7
	r	8450842	506	50	$48.7 \pm 1.4$	1.1	$2.8 \pm 1.5$	1.8	22.8	-9.8
SN 2019yz	g	4291421	25	82	$7.7 \pm 0.5$	1.0	$-2.3 \pm 2.5$	-0.9	22.3	-10.4
	r	4291422	40	116	$14.1\pm0.5$	1.0	$-2.6\pm2.8$	-0.9	22.1	-10.6
SN 2020fsb	g	2770731	27	29	$46.8 \pm 1.7$	1.0	$1.0 \pm 6.8$	0.2	21.2	-11.5
	r	2770732	30	19	$78.5 \pm 2.2$	1.1	$6.7 \pm 6.1$	1.1	21.3	-11.4
SN 2019bzd	g	3250211	20	64	$30.2 \pm 0.9$	1.6	$5.8 \pm 5.3$	1.1	21.4	-11.6
	r	3250212	37	82	$60.0 \pm 1.3$	1.0	$2.2 \pm 2.8$	0.8	22.1	-10.9
SN 2019pjs	g	5881631	159	99	$0.8 \pm 0.3$	1.0	$-0.1 \pm 1.2$	-0.1	23.0	-10.0
	r	5881632	487	107	$1.5 \pm 0.3$	1.0	$2.4 \pm 1.1$	2.1	23.1	-9.9
SN 2019enr	g	5190631	39	114	$28.3 \pm 0.8$	1.1	$-0.3 \pm 1.8$	-0.1	22.6	-10.5
CNI 2010 1	r	5190632	219	164	$52.1 \pm 1.2$	1.7	$0.3 \pm 1.4$	0.2	22.9	-10.1
SN 2018ebt	g	8291531	18	233	$2.6 \pm 0.8$	1.1	$0.5 \pm 6.5$	0.1	21.2	-11.9
SN 2020vg	g	4210311	39	20	$34.5 \pm 2.0$	1.4	$2.8 \pm 3.5$	0.8	21.9	-11.3
CNI 2010	r	4210312	60	61	$50.6 \pm 3.2$	1.4	$1.8 \pm 3.0$	0.6	22.1	-11.1
SN 2019aai	g	5840931	35	361	$13.1 \pm 1.3$	2.1	$-1.1 \pm 4.0$	-0.3	21.7	-11.4
CNI 2010 '	r	5840932	63	457	$21.4 \pm 1.3$	1.5	$-3.1 \pm 2.2$	-1.4	22.4	-10.8
SN 2018gjx	$\frac{g}{r}$	6041331 6041332	29 50	291 493	$5.7 \pm 0.7$ $10.0 \pm 0.9$	1.2 1.8	$-2.4 \pm 1.7$ $-1.9 \pm 2.2$	-1.4 $-0.9$	22.7 22.4	-10.5 $-10.8$
			201	444		1.8	$-19 \pm 11$			

Table 3 (Continued)

IAU Name	Band	FCQFID	$n_{\mathrm{early}}$	$n_{\mathrm{late}}$	Host Flux (10 <sup>-10</sup> mgy arcsec <sup>-2</sup> )	Scaling	Flux (10 <sup>-10</sup> mgy)	Sig.	Limit mag (mag)	Abs. Limit mag (mag)
	r	6551022	73	156	$3.2 \pm 0.4$	1.1	$0.6 \pm 4.1$	0.2	21.7	-11.5
SN 2020tkx	g	6841241	737	37	$0.9 \pm 0.4$	1.4	$0.2 \pm 2.9$	0.1	22.1	-11.1
	r	6841242	968	47	$1.4 \pm 0.4$	1.3	$-4.9\pm1.6$	-3.0	22.7	-10.5

Notes. Fields with early and late data. The FCQFID encodes the ZTF field ID (first three digits), the CCD ID (following two digits), the quadrant ID (second to last digit), and the filter ID (last digit), where 1 stands for the g band and 2 for the r band. Difference images with the same FCQFID have the same reference image.  $n_{\text{early}}$  is the number of images obtained more than 10 days before the SN discovery at  $t_0$  and  $n_{\text{late}}$  is the number of images available after the SN has faded to at least 23rd magnitude. The sixth column lists the host magnitude in maggies arcsec<sup>-2</sup>. The scaling factor quantifies how much the residuals scatter at different positions in the image and the errors on the flux residuals are scaled up by this factor. The following column lists the flux residuals f when subtracting late from early observations and its scaled-up error in units of maggies. They can be converted to AB magnitudes via  $m = -2.5 \times \log 10(f)$ . The third to last column shows the significance of the progenitor detection and the last two columns display the limiting magnitudes that the search reaches.

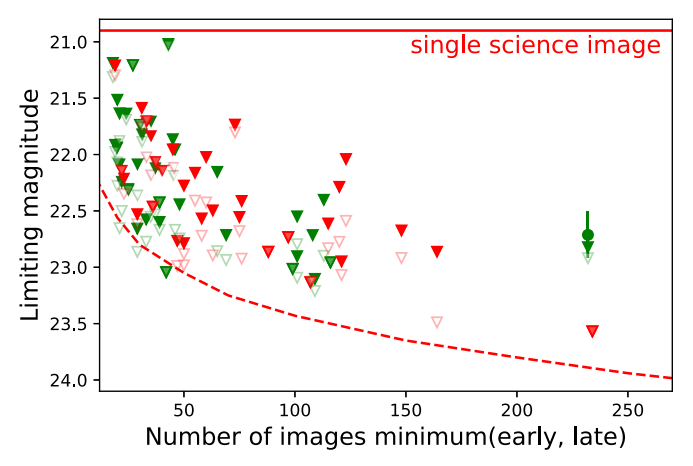


Figure 2. Apparent limiting magnitudes of the ZTF progenitor search in the g (green) and r (red) bands vs. the number of images in the time window, before or after the SN, that contains fewer ZTF images and, hence, limits the sensitivity of the search. Open triangles show the limits that are obtained with bootstrap error propagation. We then repeat our search 20 positions throughout the image and increase the error bars if the flux residuals scatter more than expected (see Appendix A.2). The resulting scaled limits are shown as solid triangles. The red dashed line indicates the ideal r-band sensitivity based on typical ZTF zero-points, sky background, and seeing values (described in Section 2.5). The limits that we obtain are less constraining due to host galaxies, nonoptimal image processing, or additional systematic errors. For comparison, the horizontal red line indicates the median r-band limiting magnitude of single difference images.

supergiant stars in the X-shooter Spectral Library (Verro et al. 2022).

Figure 3 shows the ZTF upper limits compared to detections and upper limits reported in the literature (mostly from HST). The ZTF limits are several magnitudes less sensitive than most detected progenitor stars. The upper dashed red line indicates an apparent magnitude of 23 mag, the limiting magnitude that we obtained for ZTF fields with many observations (see Section 2.3 and Table 3). Only three detected progenitors have brighter apparent magnitudes in the r band. The ZTF search would hence have a very rough detection rate of one progenitor per decade. It is sensitive to bright YSG progenitors out to  $\sim$ 20 Mpc, BSG progenitors within  $\sim$ 5 Mpc, and even closer RSGs.

One reason for the ZTF nondetections are the low RSG surface temperatures. If the adopted M4 spectral shape is typical, RSG progenitors are  $\sim$ 1.5 mag fainter in the r band compared to the F814W band. ZTF also has an i band, but the camera is less sensitive at these longer wavelengths (see Figure 12 in Masci et al. 2019) and the i band suffers from fringing.

Furthermore, it is not used as often, and the small number of observations reduces the sensitivity even further. In conclusion, the ZTF g and r bands are not red enough to detect RSG progenitors, therefore the detection of hotter, less extended progenitors such as YSG or BSG stars is more likely even though they are rarer.

#### 2.5. Expected ZTF Sensitivity

Next, we check whether the progenitor search is as good as expected for the P48 telescope or whether we lose sensitivity due to unaccounted for errors, such as registration errors or biases in the background estimation (see Appendix A.2).

We start by quantifying the sensitivity of single ZTF science images. For each science image, we look up the zero-point, ZP, and seeing, S, and measure the standard deviation,  $\sigma_{\rm bg}$ , of the sky background, B, from the image. For a source with magnitude m, the expected total number of signal counts is  $n_{\rm signal} = 10^{0.4({\rm ZP}-m)}$ . The standard deviation of the Gaussian PSF is  $\sigma = S/2.35$ . Based on Equation (1) in Ofek & Ben-Ami (2020), the expected signal-to-noise ratio (S/N) in a single image can hence be approximated as:

$$\frac{S}{N} = \sqrt{\sum \left(\frac{n_{\text{sig,pix}}}{n_{\text{bg,pix}}}\right)^2} = \frac{10^{0.4(\text{ZP}-m)}}{\sqrt{4\pi} (S/2.35) \sigma_{\text{bg}}},$$
 (1)

where  $n_{\rm sig, pix}$  and  $n_{\rm bg, pix}$  are the number of signal and background counts per pixel, respectively. We obtain the last expression by integrating over all pixels assuming a Gaussian PSF. We verify Equation (1) by injecting simulated sources and find that the S/N is 22% lower because the PSF is not perfectly Gaussian. Except for this correction, Equation (1) is a good measure for the sensitivity. To estimate the improvement when combining many images, we draw ZTF images randomly and add their S/Ns in quadrature. The resulting ideal sensitivity as a function of the number of images is shown as a dashed red line in Figure 2.

The triangles in Figure 2 represent the limiting magnitudes of the progenitor search (also given in Table 3) and they show that the sensitivity of our search is sometimes close to the ideal sensitivity, but can be up to 1.5 mag worse for other fields. The ideal sensitivity does not consider the host background which limits our search for SNe with bright hosts, such as SN 2020oi or SN 2018ivc (compare Appendix A.2). Moreover, we assume that the sensitivity is purely determined by the time window that contains the fewest observations. But if both time windows

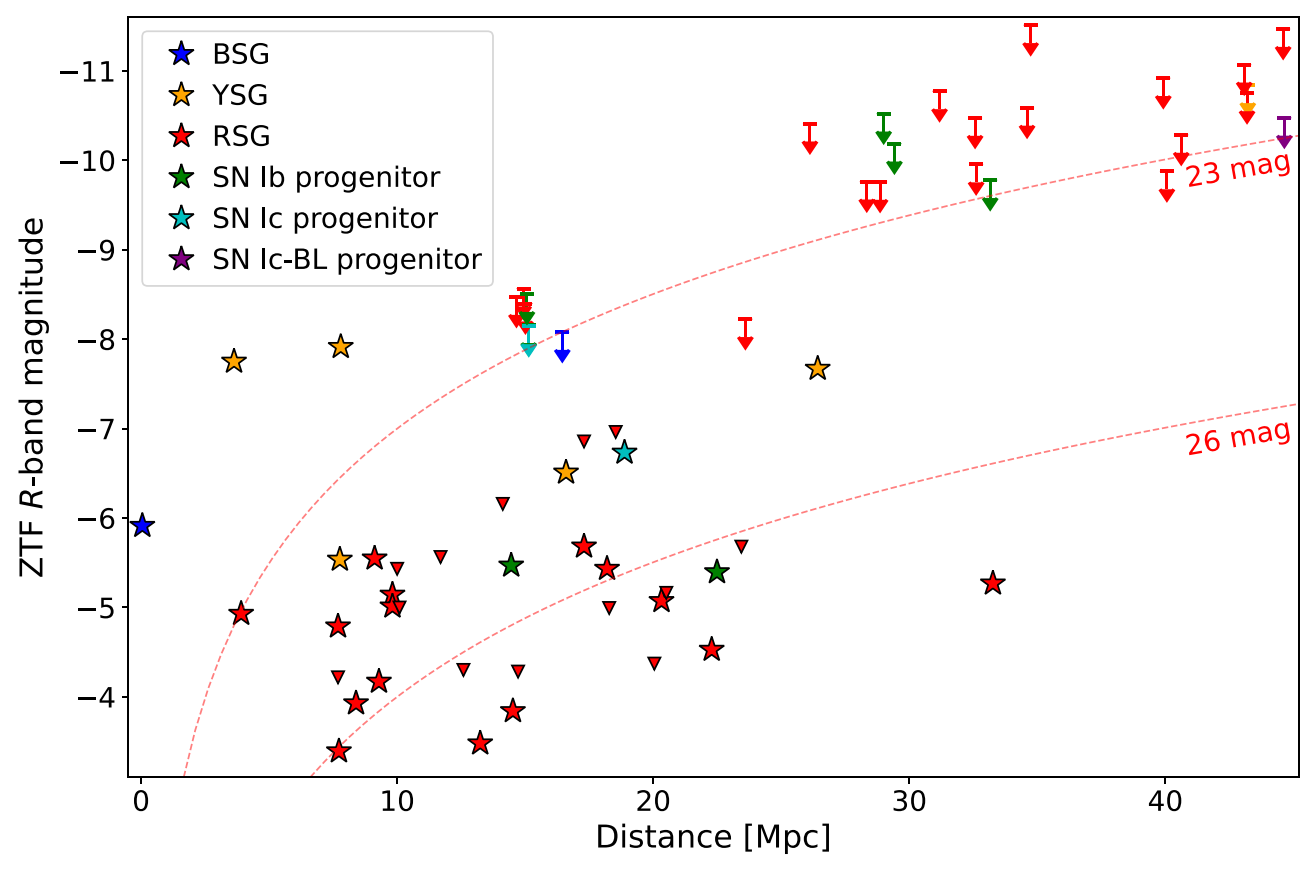


Figure 3. Arrows mark  $5\sigma$  *r*-band upper limits on the progenitor magnitudes from the ZTF search (also given in Table 3). Colors indicate the expected progenitor type based on the SN type. For comparison, we show detections (stars) and nondetections (triangles;  $3\sigma$  upper limits) of SN progenitors from the literature (listed in Tables 7 and 8). All magnitudes are converted to ZTF *r*-band AB magnitudes and we do not correct for extinction because we want to compare to the sensitivities of different surveys. Stars above the red, dashed lines are detectable in searches with limiting magnitudes of 23 mag or 26 mag, respectively.

contain the same number of observations, the sensitivity would decrease by a factor of  $\sqrt{2}$ , or by 0.36 mag. We neglect all fields where either of these effects is relevant, but find that a discrepancy remains: on average, the ZTF search could be improved by 1 mag.

Reaching the ideal sensitivity would likely require custom image coaddition and subtraction as well as a more careful calibration that reduces the scatter between epochs and between different positions within the same image. If we reach the ideal sensitivity, we would expect limiting magnitudes of 24 mag in the r band for more than 250 images in both time windows (see Figure 2). However, this is not sufficient to detect progenitors on a regular basis, as shown in Section 2.4. Thus, detecting a sample of SN progenitors requires either a larger telescope that detects more signal photons or a better site with a smaller seeing or darker sky (compare Equation (1)).

# 3. Prospects for Direct Progenitor Detections with LSST

We explore here how many progenitor detections we expect with LSST. For this purpose, we simulate a population of nearby SNe in Section 3.1 and estimate the impact of bright host galaxies in Section 3.2. We calculate the expected number of progenitor detections in Section 3.3 and discuss pre-SN outbursts in Section 3.4. Appendix B shows the bolometric corrections that we use to convert between the different spectral bands. Table 4 summarizes the LSST properties taken from Ivezić et al. (2019) and we compare them to the ZTF data analyzed in Section 2.

Table 4
Properties of the ZTF BTS Data (Analyzed in Section 2) and Assumed LSST Properties (Section 3)

	* '	<u> </u>
	ZTF BTS (r band)	LSST
Survey duration	4.6 yr	10 yr
Surveyed area	$13,000 \text{ deg}^2$	$18,000 \text{ deg}^2$
Number of visits	$110 \ {\rm yr}^{-1}$	$8/18/18 \text{ yr}^{-1} (g/r/i)$
Limiting mag. (single img.)	20.9 mag	24.9/24.7/24  mag  (g/r/i)
Limiting mag. (1 yr)	22–23 mag <sup>a</sup>	26.2/26.4/25.7  mag  (g/r/i)
Sky brightness	20.2 mag arcsec <sup>-2</sup>	21.2 mag arcsec <sup>-2</sup> $(r)$
Median seeing	2"	0."65 (r)

**Note.** The expected LSST properties are taken from Ivezić et al. (2019). <sup>a</sup> 23.3 mag expected (see Section 2.5).

# 3.1. Simulating a Population of Nearby SNe

To simulate a population of nearby SNe, we randomly draw a distance, explosion time, peak magnitude, fading time, progenitor magnitude, and the host background at the SN position.

The distances of very nearby SNe are determined by individual galaxies, as exemplified by SN 2019ehk and SN 2020oi, which exploded in the same host (see Table 1). We adopt the local galaxy distribution from the GLADE+

catalog (Dálya et al. 2022) and roughly select the part of the extragalactic sky that LSST can observe. We consider galaxies within 70 Mpc and the catalog is approximately complete out to this distance (Dálya et al. 2022). The *B*-band flux of galaxies mostly originates from young, hot stars and is closely correlated with the star formation and SN rates. We, therefore, draw the distances of the simulated SNe according to the *B*-band luminosity of galaxies in the GLADE+ catalog.

Conservatively, we only consider bright SNe with peak magnitudes of at least 18.5 mag, i.e., SNe that a survey similar to BTS would find and classify. For this purpose we draw absolute peak magnitudes from the r-band SN luminosity function presented by Perley et al. (2020), convert them to apparent magnitudes, and discard 22% of the simulated SNe that are fainter than 18.5 mag.

The SN fading time is crucial because the progenitor search requires late-time observations as we search for a vanishing source rather than trying to identify the progenitor in pre-SN images alone. In Section 2.1, we extrapolate the r-band light curves of 50 ZTF SNe. They fade to 23 mag within 0.8-2.5 yr with a median of 1.6 yr. But when extrapolating to fainter magnitudes, slower radioactive decays might start to contribute. SN 1987A is one of few SNe with very-late-time detections (Seitenzahl et al. 2014) and we here assume that all light curves develop similarly after they have reached 23 mag. Compared to a pure <sup>56</sup>Co decay, the slower <sup>57</sup>Co decay only increases the median fading time to 27.5 mag by 70 days. <sup>44</sup>Ti starts to dominate the light curve at even later times and is not relevant to our search. Slower radioactive decays hence only have a very minor impact on the progenitor search, if the ratios between the isotopes are similar to the ones for SN 1987A. SNe fade to 27.5 mag within 1.9-6 yr with a median duration of 3 yr.

We caution that some SNe might fade away more slowly especially in the optical bands: most SNe in the sample by Rizzo Smith et al. (2023) did not fade below their progenitor magnitude for a decade. However, in infrared bands, where RSG progenitors are brighter, the disappearance of progenitor stars has been confirmed for many SNe (see, e.g., Van Dyk et al. 2023). Slower fading rates can, for example, be caused by late-time interaction with a circumstellar medium (see, e.g., Sollerman et al. 2020 for extreme examples; Weil et al. 2020), light echoes (Maund 2019), or prolonged magnetar emission. The LSST cadence will allow monitoring of the SN fading rates at least as long as they are detectable in single images. Of all SNe that explode during the 10 yr survey 80% fade to at least 24.7 mag before the end of the survey, i.e., they are no longer detectable in single LSST images. Within the survey footprint, LSST is scheduled to collect 184 r- and i-band observations (Ivezić et al. 2019), while 80 g-band visits are planned. SNe that are bright in the middle of the survey have 60 to 80 LSST r- and i-band images both before and after the SN. However, SNe that happen earlier or later have fewer observations in one of the time windows, resulting in a lower sensitivity (compare Figure 2). As a consequence, the average SN has 35 r- and iband and 16 g-band observations in the shorter time window.

Finally, we draw absorbed *i*-band magnitudes for RSG progenitors from the luminosity function of Davies & Beasor (2020) and convert them to LSST g-, r-, and i-band magnitudes using the bolometric corrections given in Appendix B.

#### 3.2. The Impact of Bright Hosts on the LSST Sensitivity

The designed limiting magnitude of a single LSST visit is 24.7 mag in the *r* band (Table 1 of Ivezić et al. 2019) while the expected limiting magnitude after 10 yr and 184 observations is 27.5 mag. Figure 2 in Ivezić et al. (2019) shows how the sensitivity improves when coadding several *r*-band observations. The improvement is similar for *g*- and *i*-band images, but *g*-band observations are 0.2 mag deeper while *i*-band observations are 0.7 mag less constraining (Ivezić et al. 2019). The LSST *z* and *y* bands can likely also be used for progenitor searches and RSGs are bright in these bands (see Appendix B). However, the SN fading times might be longer, e.g., due to dust formation, and we, therefore, do not consider these bands here.

However, the limiting magnitudes quoted by Ivezić et al. (2019) are only valid for isolated sources. In such locations, the background is dominated by the sky brightness of on average 21.2 mag arcsec<sup>-2</sup> in the LSST r band (Table 2 by Ivezić et al. 2019) or  $3.3 \times 10^{-9}$  maggies arcsec<sup>-2</sup>. But many SNe explode on top of bright host galaxies. As shown in Equation (1), the S/N is proportional to  $\sigma_{\rm bg}^{-1}$  and the standard deviation of the sky background is  $\sigma_{\rm bg} = B^{-0.5}$  where B is the sum of all relevant backgrounds at the SN position. The host background, therefore, degrades the limiting magnitude by:

$$\Delta l = 1.25 \log 10 \left( 1 + \frac{B_{\text{host}}}{B_{\text{sky}}} \right), \tag{2}$$

where  $B_{\text{host}}$  and  $B_{\text{sky}}$  are the host and sky background in counts per area, respectively.

In Section 2.2, we measured the *r*-band host surface brightnesses at the positions of 29 ZTF SNe using late-time ZTF data (see Table 3; details on the calculation are described in Appendix A.2). We assume that LSST SNe will explode in similarly bright galaxies and randomly draw host backgrounds from this distribution. To first order, the host surface brightness is independent of the distance: nearby galaxies are brighter, but they are also more resolved, such that the number of photons per pixel is roughly preserved. We use Equation (2) to calculate by how much these hosts would reduce the sensitivity of our search in LSST data. Figure 4 shows that 46% of the galaxies are brighter than the average LSST sky background, i.e., the host background reduces the limiting magnitude by more than 0.38 mag and for 7% of the hosts the sensitivity is reduced by more than 1 mag.

Compared to LSST, ZTF is less affected by host backgrounds because the sky background is on average 1 mag arcsec<sup>-2</sup> brighter than at the LSST site. Nevertheless, the ZTF search is host dominated for 14%, or four of the 29 SNe in our sample: the host backgrounds of SN 2019yvr, SN 2020oi, and SN 2020fqv are larger than the average sky background and the bright host of SN 2018ivc produces large residuals during image subtraction, such that quality cuts reject most of its *r*-band observations (compare Appendix A.2).

Even the brightest host galaxies are most likely not saturated in LSST images. For a seeing of 0.77 and an exposure time of 15 s, a point source is saturated if it is brighter than 15.8 mag in the r band (Abell et al. 2009). For this seeing and the LSST pixel size (Ivezić et al. 2019) about 10% of the photons fall on the brightest pixel. An extended source, like a galaxy, produces as many photons per pixel if it has a surface brightness of 14.8 mag arcsec<sup>-2</sup>. In the ZTF sample, SN 2020oi has the

Table 5
Expected Number of LSST Detections for Different Progenitor Types

Туре	Fraction	#SNe	Progenitor Lum.	Spectral Type	# Detections			
		11	$(\text{mag}_i)$	71	g	r	i	
RSG	0.56	273	LF	M4	1.4	17	46	
				M2	5.4	44	72	
YSG	0.09	44	-5.4	A5	2.4	5.2	1.6	
BSG	0.02	9.8	-5.6	B2	0.95	2.3	0.5	
SN Ib progenitor	0.12	56	≤−4.7	F2	≥0.87	≥1.0	≥0.79	
SN Ic progenitor	0.14	66	≤−4.0	A5	≥0.57	≥1.0	≥0.44	

Notes. The number of SNe within 70 Mpc with both pre-SN and late-time observations during the 10 yr survey for 18,000 deg<sup>2</sup>. The SN fractions in the second column are taken from Li et al. (2011) and Kleiser et al. (2011). For RSGs, the progenitor i-band magnitudes are drawn from the luminosity function of Davies & Beasor (2020). Due to the lack of a measured luminosity function, we assume that all YSGs are as bright as the progenitor of SN 2008ax and BSGs as the one of SN 1987A (fourth column of the table; taken from Table 8). The luminosities of SN Ib and SN Ic progenitors are highly uncertain, but we expect at least one LSST detection if they are brighter than -4.7 and -4.0 mag in the i band, respectively. In addition, we assume that the SN fading rates and host luminosities are similar to the ZTF sample (Section 2).

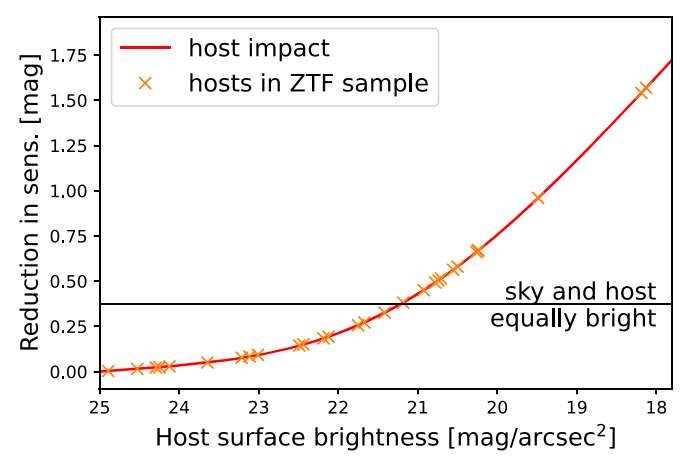


**Figure 4.** Reduction in the limiting magnitude due to the host background for the expected LSST sky background of 21.2 mag arcsec<sup>-2</sup>. The orange crosses indicate the *r*-band host backgrounds at the locations of 29 nearby ZTF SNe (see Section 2).

brightest host background with 18.1 mag arcsec<sup>-2</sup>, and is hence a factor of 20 fainter than the LSST saturation limit for extended sources.

# 3.3. Expected LSST Progenitor Detections

LSST is planning to monitor 18,000  $\deg^2$  of extragalactic sky over 10 yr in the *ugrizy* filters (Ivezić et al. 2019). For an SN rate of  $10^{-4}$  Mpc<sup>-3</sup> yr<sup>-1</sup> (Perley et al. 2020) and the distribution of nearby galaxies (Dálya et al. 2022), we expect in total  $\sim$ 600 SNe within 70 Mpc. Out of these, 490 have peak magnitudes brighter than 18.5 mag in the *g* or *r* bands and fade within the survey duration to at least 24.7 mag in the *r* band. 56%, or about 270 of them, are SNe II with RSG progenitors (Li et al. 2011).

Next, we convert the available number of LSST images, calculated in Section 3.1, to limiting magnitudes while also considering the impact of the host background as described in Section 3.2. The most constraining limits are  $\sim$ 27.2 mag in the r band for SNe that have 70 LSST observations both before and after the SN. However, the median SN only has half as many observations in the shorter time window and the median limiting magnitude is, therefore, 26.2 mag in the r band and 25.9 and 25.8 mag in the g and g bands, respectively.

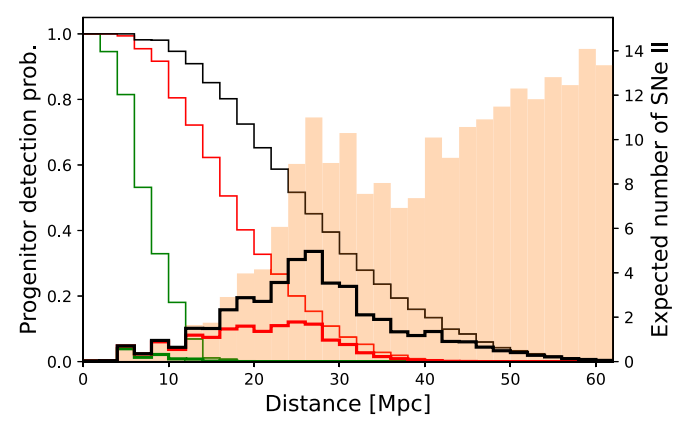


**Figure 5.** Probability that an RSG progenitor with an M4 spectrum is detected in the LSST g (thin green line), r (red), or i (black) band and the expected number of bright, nearby SNe within the LSST footprint during the 10 yr survey (orange distribution; right axis). The number of progenitor detections is given as the product of the two (thick lines; right axis) and we expect 46 RSG detections in the i band, 17 in the r band, and 1.4 in the g band.

Figure 5 shows the distance distribution of the closest SNe (orange distribution) and their detection probability in the LSST g, r, and i bands. For the i band the detection probability is close to one out to  $\sim 10$  Mpc, i.e., even faint progenitor stars are detected within this distance. In the g band, on the other hand, progenitors are so faint that they might remain undetected even for the closest SNe. The total expected number of RSG detections is given by the sum over the distribution: we expect about 46 RSG progenitor detections in the i band, 17 in the r band, and 1.4 in the g band, if the stars have M4 spectra (see Table 5). Neglecting the host background (see Section 3.2) would have yielded 56 *i*-band detections, e.g.,  $\sim$ 30% of the RSG progenitors remain undetected due to their bright host galaxies. For a less red M2 spectrum, we expect 72, 44, and 5 detections in the i, r, and g bands, respectively. LSST is hence sensitive to the surface temperature and we expect more detections for slightly hotter progenitors.

Our search will also produce strong constraints for the high-luminosity end of the RSG luminosity function. The brightest detected RSG so far is SN 2012ec with a bolometric magnitude of -8.11 mag (compare Table 7), corresponding to an LSST *i*-band magnitude of -7.28 mag. We expect that 100 LSST searches will be sensitive to as bright progenitor stars. These

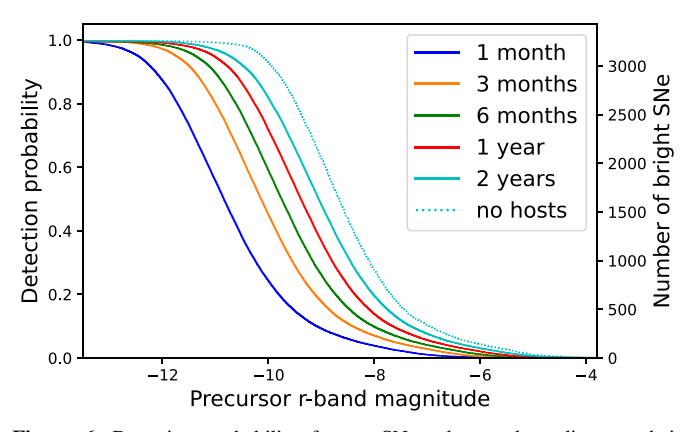


**Figure 6.** Detection probability for pre-SN outbursts depending on their luminosity and duration. The calculation was done for a population of SNe with peak luminosities brighter than 18.5 mag and the right-hand axis shows the expected number of core-collapse SNe within the LSST footprint during the 10 yr survey. The dotted, cyan line indicates that the average host galaxy reduces our sensitivity by 0.4 mag (see also Figure 4).

observations can help to establish whether a significant RSG problem is present.

LSST will also detect non-RSG progenitors. Table 5 lists the expected number of SNe within 70 Mpc based on the volumetric SN fractions of Li et al. (2011) and Kleiser et al. (2011). The luminosity functions of these progenitor types are not well constrained, and we, therefore, assume that all YSGs are as bright as the progenitor of SN 2008ax (see Table 8); for BSGs we adopt the magnitude and spectrum of the progenitor of SN 1987A. The last three columns of Table 5 show that we expect the detection of  $\sim$ two YSG and two BSG progenitors. In addition, we expect the detection of at least one SN Ib progenitor if they are brighter than -4.7 mag in the i band, and SN Ic progenitors become detectable if they are at least as bright as -4.0 mag.

# 3.4. LSST Detection Rates for Pre-SN Eruptions

The impending core collapse can trigger pre-SN outbursts. These eruptions are well observed for SNe IIn (Ofek et al. 2014; Strotjohann et al. 2021), but also happen prior to other types of SNe (see, e.g., Ho et al. 2019; Jacobson-Galán et al. 2022a). We here estimate rough LSST detection rates for outbursts that happen immediately before the SN explosion.

Bright outbursts can be detected even for distant SNe and we assume a homogeneous SN rate of  $10^{-4}~\rm Mpc^{-3}~\rm yr^{-1}$  for distances larger than 70 Mpc where the GLADE+ galaxy catalog is incomplete. As before, we only consider SNe with peak magnitudes brighter than 18.5 mag. Within the 10 yr LSST survey, we expect the detection of 3300 as bright corecollapse SNe and they are located at a median distance of 120 Mpc.

Figure 6 shows our sensitivity to precursor eruptions depending on the outburst magnitude and duration. One month long outbursts are typically only present in one or two LSST r-band images and LSST can detect half of them if they are brighter than an absolute magnitude of -10.3 mag. Longer-lasting outbursts are observed several times and combining several epochs increases our sensitivity. We search for outbursts as described in Section 3.2. The only difference is that we compare observations obtained a few months or years before the SN to earlier pre-SN observations. and for For a 2 yr long eruption, the median sensitivity improves to -9.0 mag.

The dotted, cyan line in Figure 6 visualizes that the average host reduces our sensitivity by 0.4 mag (see also Figure 4).

SNe IIn make up about 9% of all core-collapse SNe (Perley et al. 2020) and LSST will detect  $\sim\!300$  SNe IIn with peak magnitudes brighter than 18.5 mag. Strotjohann et al. (2021) found that 25% of the progenitors have outbursts brighter than -13 mag and Figure 6 shows that as bright outbursts are detectable even in single LSST images. Therefore, we expect the detection of at least 75 such outbursts. A four month long outburst with a faint, absolute magnitude of -11.3 mag was detected prior to SN 2020tlf, an SN II with long-lasting flash-spectroscopy features (Jacobson-Galán et al. 2022a). We expect the detection of 1800 bright SNe II and similar outbursts would be detectable for 90% of them. This large number of bright SNe will allow us to measure the rate, luminosity function, and timing of the outbursts, which might contribute to revealing their triggering mechanism.

#### 4. Conclusion

We propose searching for SN progenitor stars by combining a large number of images from ground-based, wide-field surveys to detect the star's disappearance. The advantages of this approach are that the data are readily available and collected systematically for a large fraction of the sky, usually in several bands, and late-time data ensure that the progenitor star has indeed vanished.

We test the proposed method by searching for the progenitor stars of 29 ZTF SNe with redshifts z < 0.01 that have already faded sufficiently (see Section 2). We combine up to a few hundred observations before and after the SN and subtract the fluxes in these two time windows from each other. With the available amount of data, the backgrounds from host galaxies, and statistical and systematic errors in ZTF difference images, we reach limiting magnitudes down to  $\sim$ 23 mag in the g and r bands. We do not detect any progenitor stars or long-lasting outbursts and detections reported in the literature are typically several magnitudes fainter than our limits (see Section 2.4). We estimate that ZTF is sensitive to the brightest YSGs and to the closest RSGs within 5 Mpc, which yields a detection rate of approximately one per decade. Additional data would likely improve the limiting magnitude for some fields, while others seem limited by various errors. Our search is, on average, 1 mag less sensitive than expected for a ZTF-like survey, in part presumably because we combined relatively shallow difference images instead of producing dedicated difference images. Our method hence requires precise photometric calibration, longterm stability, and potentially improved image coaddition and source detection methods.

In Section 3, we quantify the expected number of progenitor detections with the upcoming LSST survey, assuming that the survey reaches its design specifications. We carefully consider the increased background due to bright host galaxies, but presume that they do not create residuals or other systematic errors during image subtraction. We can mitigate such errors empirically, as done for ZTF in Section 2.3. However, this would reduce the sensitivity of our search.

We estimate that LSST will yield 50–70 RSG progenitor detections. For half of the RSG progenitors, r-i colors will allow us to constrain the surface temperature and distinguish between M2- and M4-type stars, reducing the statistical and systematic errors on the RSG luminosity function. The larger sample of RSG progenitors with measured bolometric

corrections might help to establish whether the RSG problem is significant (the impact of bolometric corrections is shown by Davies & Beasor 2018).

We also expect to detect several YSG and BSG progenitors (see Table 5), but the number of detections is highly uncertain due to the unknown luminosity functions and surface temperatures and due to statistical fluctuations. The detection of SNe Ib and Ic progenitors is possible if their LSST *i*-band magnitudes are brighter than -4.7 and -4.0 mag, respectively. The progenitors of stripped-envelope SNe could either be stripped by binary partners, or they could be very massive stars with strong winds, and progenitor detections in several bands might allow us to distinguish between these two scenarios. Wu & Fuller (2022) predict that late nuclear burning stages trigger mass loss and brightening for stripped stars. Such events would boost the detection rate for these progenitors and offer direct information about the processes in their stellar cores.

LSST pre-SN light curves will be sensitive to precursor eruptions that could produce confined shells of material around the star (see, e.g., Tsuna et al. 2023). Increased mass loss is required to explain both flash-spectroscopy features (see, e.g., Bruch et al. 2023) and early SN light curves (Förster et al. 2018; Morozova et al. 2020), but it is so far unclear how the star produces this environment (see, e.g., Davies et al. 2022). We expect the detection of more than 70 bright outbursts prior to SNe IIn and many RSG outbursts if they are common and brighter than -9 mag. In addition, low-amplitude variability or dimming events, for example observed by Szczygiełet al. (2012) and Rui et al. (2019), can be detected for the brightest progenitors.

In summary, we show that the planned LSST survey is well suited to detect both quiescent and flaring SN progenitor stars and might therefore provide answers to several open questions concerning the last evolutionary stages of massive stars.

#### Acknowledgments

We thank the anonymous referee, Schuyler Van Dyk, and Doron Kushnir for their comments on the manuscript. In addition, we are grateful to Morgan Fraser, Emma Beasor, Samantha Wu, Azalee Bostroem, Eva Laplace, and Dietrich Baade for helpful discussions. We would like to thank the organizers of the MIAPbP workshop on interacting supernovae.

N.L.S. is funded by the Deutsche Forschungsgemeinschaft (DFG, German Research Foundation) via the Walter Benjamin program—461903330. This research was supported by the Munich Institute for Astro-, Particle and BioPhysics (MIAPbP), which is funded by the Deutsche Forschungsgemeinschaft under Germany's Excellence Strategy—EXC-2094—390783311.

E.O.O. is grateful for the support of grants from the Benozio center, Willner Family Leadership Institute, Ilan Gluzman (Secaucus NJ), Madame Olga Klein—Astrachan, Minerva foundation, Israel Science Foundation, BSF, Israel Ministry of Science, Yeda-Sela, and Weizmann-MIT.

This work is based on observations obtained with the Samuel Oschin Telescope 48 inch and the 60 inch Telescope at the Palomar Observatory as part of the Zwicky Transient Facility (ZTF) project. ZTF is supported by the National Science Foundation under grants No. AST-1440341 and AST-2034437, and a collaboration including current partners Caltech, IPAC, the Weizmann Institute of Science, the Oskar Klein Center at Stockholm University, the University of Maryland, Deutsches

Elektronen-Synchrotron and Humboldt University, the TANGO Consortium of Taiwan, the University of Wisconsin at Milwaukee, Trinity College Dublin, Lawrence Livermore National Laboratories, IN2P3, University of Warwick, Ruhr University Bochum, Northwestern University and former partners the University of Washington, Los Alamos National Laboratories, and Lawrence Berkeley National Laboratories. Operations are conducted by COO, IPAC, and UW.

This research has made use of the NASA/IPAC Extragalactic Database (NED), which is funded by the National Aeronautics and Space Administration and operated by the California Institute of Technology.

This research has used the Spanish Virtual Observatory (https://svo.cab.inta-csic.es) project funded by MCIN/AEI/10.13039/501100011033/ through grant PID2020-112949GB-I00.

# Appendix A ZTF Search

# A.1. Forced-photometry Pipeline and Quality Cuts

Instead of implementing our own image subtraction algorithm, we rely on difference images created by IPAC (Masci et al. 2019) based on the ZOGY algorithm (Zackay et al. 2016). IPAC difference images are based on relatively shallow reference images that were produced by coadding 15–20 images. We download the IPAC difference images, their associated PSFs, and reference images using the *ztfquery* package (Rigault 2018) and calculate forced-photometry light curves for all SNe.

We first determine the exact SN position by calculating the median R.A. and decl. of all ZTF alerts (Patterson et al. 2019) that were issued for the SN. Our forced-photometry pipeline is a modified version of the pipeline written by Yao et al. (2019), also used by Strotjohann et al. (2021). As demonstrated by Strotjohann et al. (2021), 50 Markov Chain Monte Carlo walkers yield a sufficiently precise flux measurement. The results are similar to light curves produced by the ZTF forced-photometry service (Masci et al. 2019), but our pipeline returns additional parameters that we use for quality cuts.

After calculating the SN light curves, we reject less reliable data points according to the following criteria: (1) flagged images (i.e., the INFOBITS keyword in the header is not zero), (2) images with large residuals in the background region (a background standard deviation of >25 counts), (3) images with bad pixels within the  $7 \times 7$  pixels around the SN position, (4) images with a seeing of >4'', (5) images with intermittent clouds that are flagged in the IPAC metadata tables, <sup>15</sup> and (6) images based on deleted reference images. A few ZTF reference images were accidentally overwritten, such that later difference images are based on a new, different reference image. To avoid combining observations with different reference images we discard any difference images that were created earlier than the available reference image. All quality cuts and their impact on the amount of data are listed in Table 6 and the fluxes of all observations that pass our quality cuts are given in Table 2.

ZTF i-band observations are on average one magnitude less sensitive compared to the g and r bands and the images suffer

<sup>&</sup>lt;sup>15</sup> As described in https://web.ipac.caltech.edu/staff/fmasci/ztf/extended\_cautionary\_notes.pdf. The flag is only present in the meta tables because the image headers are written earlier.

**Table 6**Quality Cuts for ZTF Data

	Cut	Discarded Frac.	Remaining Obs.
	Before cuts	•••	35,120
1	Flagged images	5.8%	33,081
2	Bkg. std $> 25$ counts	2.9%	32,106
3	Bad pixels	0.1%	32,082
4	Seeing $\geqslant 4''$	2.5%	31,285
5	Cloudiness parameter	1.4%	30,848
6	Reference overwritten	2.8%	29,981
7	<15 pre-SN images	2.3%	29,305

from fringing. Therefore, we discard them here even though the *i*-band fluxes of RSGs are typically  $\sim$ 1.5 mag brighter than their *r*-band fluxes (see Section 2.4).

Like Yao et al. (2019), we use the zero-points from the image headers to calculate fluxes f in units of maggies. These are converted to asinh magnitudes (Lupton et al. 1999) via:

$$m_{AB} = -2.5/\ln(10)(\arcsin(f/2b) + \ln(b)),$$
 (A1)

$$\Delta m_{\rm AB} = 2.5/\ln(10) \times \Delta f/f,\tag{A2}$$

$$l_{AB} = -2.5 \log(5 \times \Delta f), \tag{A3}$$

with a softening parameter  $b = 10^{-10}$ . If the calculated magnitude is brighter than the limiting magnitude, the source is detected at the  $5\sigma$  level. Otherwise, we use the  $5\sigma$  upper limit as a nondetection, and the magnitude does not have a physical meaning (Lupton et al. 1999).

In the following, we only consider objects with at least 20 pre-SN observations per field. For these sources, we do a baseline correction, to ensure that the weighted mean pre-SN flux is zero. This is done separately for each field or reference image, i.e., for observations with the same combination of ZTF field, CCD, quadrant, and filter. We use the baseline correction only to calculate the SN fading time in Section 2.1. When searching for progenitors in Section 2.2 we subtract late from early fluxes, such that the baseline correction cancels out.

To check whether the errors of the flux can account for the scatter of the preexplosion light curve, we calculate the reduced  $\chi^2$  relative to the zero-flux level. If the result is larger than one, the flux errors are likely underestimated and we scale them up such that the reduced  $\chi^2$  reaches one. If the reduced  $\chi^2$  is smaller than one, the error bars are potentially too large and we do not modify them. The corrections are generally small with factors close to one.

For the sample selection, described in Section 2.1, we bin light curves in 7 day bins and also combine fluxes with different reference images. We use the median observation time as the time of the binned data point. The flux per bin is the mean flux weighted by the flux errors and the error on the flux is calculated via error propagation because many bins do not contain enough data points to calculate bootstrap errors (Efron 1982). We make sure that observations before and after the estimated explosion date are never combined in the same bin.

# A.2. Additional Error Sources in ZTF Images

One major error source for our analysis are bright host galaxies, which can impact our search in several ways as image subtractions do not always work well for these environments. One effect is that the higher source noise increases the statistical errors in each pixel (as quantified in Section 3.2).

This higher background results in larger errors when fitting the flux and is therefore considered automatically by the forced-photometry pipeline. SN 2020oi and SN 2018ivc have the brightest hosts (see Table 3), and Figure 1 shows that the typical flux upper limits are less constraining compared to the other SNe in the sample.

In addition to increased source noise, bright hosts can cause photometric errors or residuals in difference images that are harder to quantify. Both registration errors, i.e., misalignments by a fraction of a pixel, and errors on the gain are more severe in such locations as the large fluxes in the science and reference images are subtracted from each other. We find that our quality cuts are to some degree sensitive to these problems: for positions on top of a bright galaxy such as SN 2018ivc, most r-band observations are rejected, because they have poor PSF fits with a reduced  $\chi^2 > 1.4$ .

When searching for progenitor stars, we are comparing observations that were obtained several years apart and we observe for some sources that the residuals become larger due to long-term changes. This is also observed for SN 2020cxd (see Figure A1), for which the background flux decreases both before and after the SN. We do not detect similar trends at other positions in the galaxy and it might be caused by a background source. Another error source is the rather shallow reference images. In the progenitor search, we are trying to detect sources that are potentially fainter than the limiting magnitude of the reference image. In our search, we only compare difference images that were produced with the same reference image, such that the reference's impact cancels out to first order. However, when producing difference images the reference is convoluted with the PSF of the science image, which could introduce residuals, e.g., if the average seeing is different in preexplosion images compared to late-time images. To mitigate the impact of these errors empirically, we repeat the progenitor search for 20 positions in the field where the host is similarly bright and if the resulting residuals are larger than expected, we scale up the error bars.

First, we measure the host flux at the SN position. Some reference images contain SN light and, therefore, we measure the host flux in late-time science images instead. For each field, we download 25 science images that are not flagged, have a limiting magnitude of more than 19.5 mag, and a seeing of <4''. Then, we measure the sky background in a  $600 \times 600$ pixel region around the SN position. We reject  $2\sigma$  outliers to remove any sources in the image and calculate the median count rate for the remaining pixels. We then determine the host flux by calculating the median flux of the  $7 \times 7$  pixels around the SN position, the same pixels that are used for the PSF fit, and we subtract the sky background from it. To obtain a result in physical units, we convert the fluxes to maggies using the zero-point from the image header (Masci et al. 2019) and we normalize it to units of flux arcsecond<sup>-2</sup>. In Table 3 we quote the median host flux of all 25 late-time images as the host flux and use the standard deviation as the uncertainty on the flux.

Next, we select positions within the same host galaxy that have similar fluxes. For this purpose, we take a Cartesian grid of positions with separations of 7 pixels and  $21 \times 21$  points. We estimate the host flux at each of these positions as described above and select the 20 positions with the flux that is closest to the flux at the SN position. Then, we obtain forced-photometry light curves for each position and run the progenitor search.

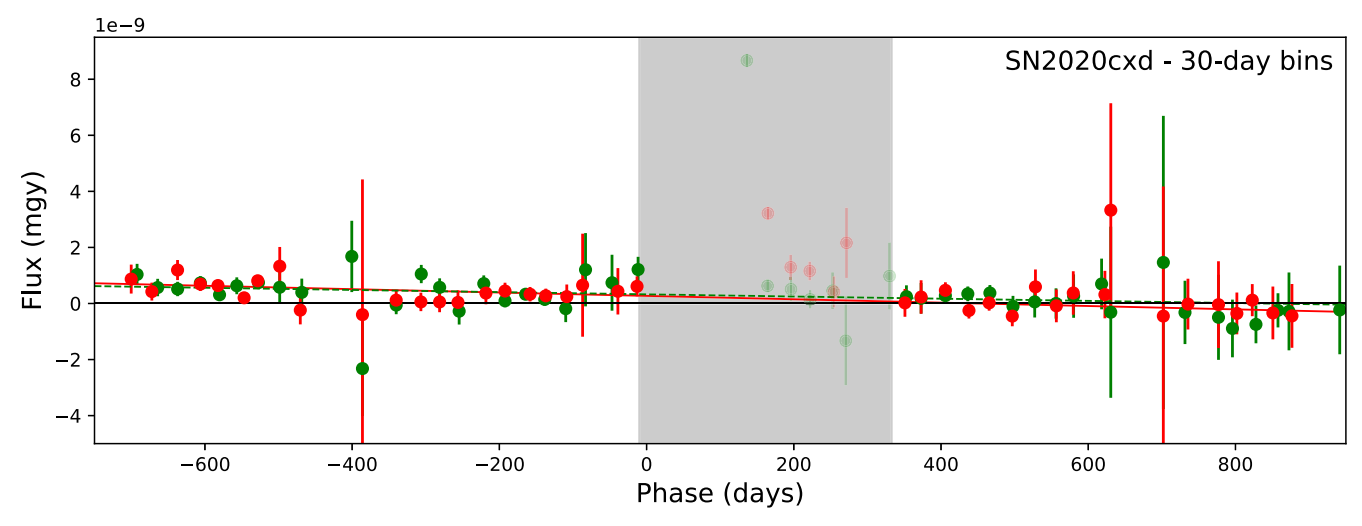


**Figure A1.** Variability at the position of SN 2020cxd. We fit a straight line to the *g*- and *r*-band observations, excluding the SN itself (gray shaded area) and find that the fluxes in both bands decrease over the duration of the survey. The trend appears to continue after the SN and, therefore, we conclude that it is unrelated to the progenitor star. No similar variability was observed for 20 nearby positions in the same host galaxy.

Each of the 20 background positions yields a flux residual, the early-time minus the late-time flux, and we calculate the standard deviation of these 20 residuals. If it is close to one the size of the error bars is appropriate, but if it is larger than one the residuals scatter more than expected and we scale up the error bars by the size of the standard deviation. All scaling factors are given in the seventh column of Table 3 and they are typically close to one. For SN 2018ivc, the scaling factor is close to two due to its bright host and a few other fields also have relatively high scaling factors, but we cannot identify any obvious reason(s) for these.

## A.3. Simulated Sources

To verify our sensitivity we inject point sources into the ZTF images and rerun the search to check whether these sources are detected significantly. To save computational time, we do this test only for two fields that include SN 2018hna, 8190141 and 8190142, which yield deep limits in the g and r bands (see Table 3).

We simulate progenitors at the same 20 positions that we use to construct the background data set in Appendix A.2. When simulating a point source with a certain magnitude in a given image, we first calculate the expected number of photons based on the zero-point and exposure time and simulate a Gaussian with the width of the measured seeing. We also consider atmospheric scintillations, which shift the point source by the fraction of a pixel (the rms displacement is given by Equation (51) in Zackay et al. 2016). We inject sources of various luminosities into the preexplosion images, run the progenitor search, and check whether the simulated progenitors are detected with a significance of  $5\sigma$ .

Figure A2 shows that we obtain  $5\sigma$  detections if the progenitor is brighter than -7.5 to -8.25 mag in the g and r bands, respectively. At the actual SN position, we measured  $5\sigma$  limiting magnitudes of -8.1 and -8.3 mag in the g and r bands, respectively (see also Table 3 and Section 2.3). The limit that the progenitor search returns is, hence, comparable to the magnitudes at which we can detect simulated sources in the same field. We, therefore, conclude that the quoted limiting magnitudes are realistic. The dashed lines in the figure show that the  $3\sigma$  limiting magnitudes would be  $\sim$ 0.7 mag more

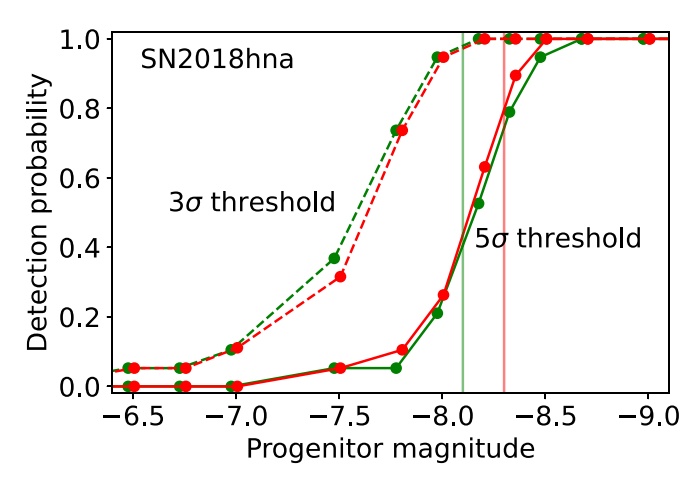


**Figure A2.** To confirm the sensitivity of our search, we simulate progenitor stars at 20 positions close to the location of SN 2018hna that have similar host fluxes. The solid curves in the figure display the fraction of positions for which our search achieves  $5\sigma$  detections. The two vertical lines show that the limits we obtained at the true SN position are comparable. A  $3\sigma$  threshold (dashed lines) would increase the sensitivity by  $\sim$ 0.7 mag, but might yield false detections.

constraining. However, we here maintain the  $5\sigma$  threshold to avoid false detections.

# Appendix B Converting between Different Spectral Bands

Converting between different spectral bands requires assuming a spectral shape. We use observed stellar spectra from the third data release of the X-shooter spectral library (XSL;<sup>16</sup> Verro et al. 2022). We only select dereddened spectra that are corrected for slit losses and have data over the entire wavelength range. We interpolate over telluric bands and chip gaps (wavelength ranges given in Figure A.3 in Lançon et al. 2021) with a quadratic spline function. Supergiant spectra are not available for the coolest RSGs (more evolved than type M5) and we use giant spectra instead. We calculate bolometric magnitudes by integrating the XSL spectra between 3500 and

http://xsl.u-strasbg.fr

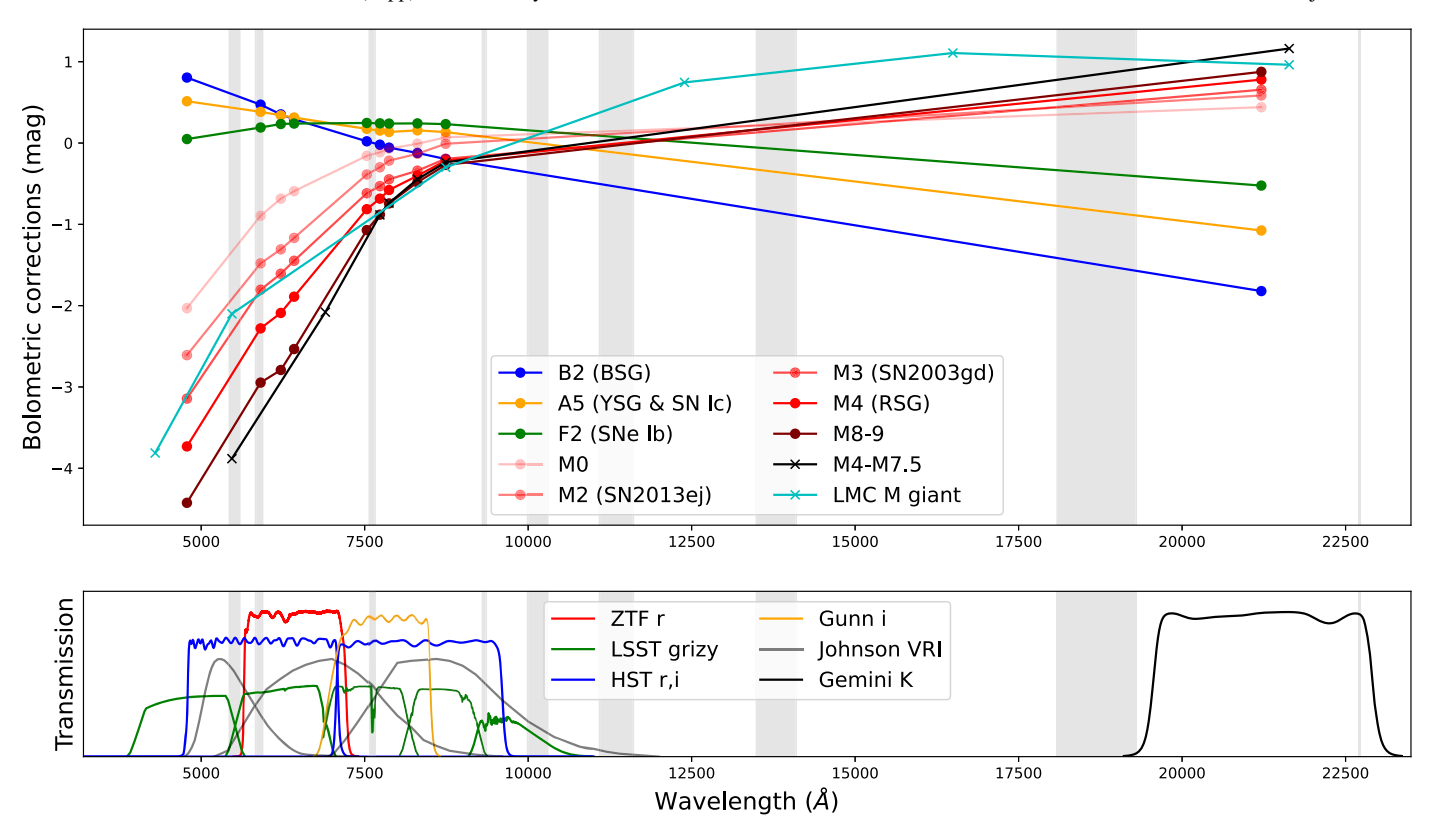


**Figure B1.** Bolometric corrections based on XSL giant and supergiant spectra. Gray shaded bands mark X-shooter chip gaps and the telluric bands over which we interpolate. In addition, we show the bolometric corrections of Davies & Beasor (2018) as a black line and the average LMC M supergiant corrections in cyan. We use AB magnitudes throughout the paper. They can be converted to Vega magnitudes by subtracting 0.085 (F606W), 0.181 (ZTF r), 0.394 (i'), 0.418 ( $I_C$ ), 0.445 (F814W), 0.487 ( $I_J$ ), or 1.798 mag ( $I_J$ ).

24800 Å and single-band magnitudes by integrating over the spectrum multiplied by the filter profile. Figure B1 shows the resulting bolometric corrections for supergiant and giant stars of different spectral types.

We assume that BSG progenitors have spectra similar to B2 stars (Walborn et al. 1989). For the YSG progenitors of SNe IIb we adopt an A5 star spectrum (Kilpatrick et al. 2022), and Kilpatrick et al. (2021) found the only detected SN Ic progenitor has a similar V-I color. The progenitors of SNe Ib are assumed to be similar to F2 stars (Xiang et al. 2019). We caution that the true spectral shapes are largely unknown, such that the resulting bolometric corrections have large uncertainties.

Davies & Beasor (2018) carefully consider the temperatures of RSG progenitors and conclude that they are most similar to the reddest RSGs. Davies & Beasor (2018), therefore, adopt an average M4–M7.5-type spectrum. However, none of the M-type supergiants in the XSL are as red (compare Figure B1). Instead of picking the reddest RSG in the catalog

(shown as a dark red line in Figure B1), we adopt the spectrum of a slightly hotter M4 star for all RSGs, except for the progenitors of SN 2003gd and SN 2013ej, for which we assume M3 and M2 spectra, respectively, following Davies & Beasor (2018). The spread of the red lines in Figure B1 illustrates the size of the uncertainty for the entire range of M-type giants. Most RSG progenitors are detected in the F814W band where the bolometric corrections differ by up to 0.5 mag between M supergiants of different types. However, the impact of the unknown progenitor temperatures is much larger in the *r* band, where cooler M9 stars are 2 mag fainter than M0 supergiants. As a consequence, RSG observations in the *r* band, including the ZTF data analyzed in Section 2, have highly uncertain bolometric magnitudes.

#### Appendix C

Tables 7 and 8 list progenitor detections from the literature.

 Table 7

 Limits and Detections of RSG Progenitor Stars from the Literature

SN	Dist. Mod. (mag)	E(B - V) (mag)	Band	Mag (mag)	Bol. Mag (mag)	Faded?	References
SN 1999an	31.3	0.11	F606W	>24.78	>-9.11		1, 2
SN 1999br	30.8	0.02	F606W	>24.98	>-8.08		1, 2
SN 1999em	30.3	0.09	$I_c$	>23.42	>-7.66		1, 2
SN 1999gi	30.0	0.17	F606W	>24.98	>-7.74		1, 2
SN 2001du	31.3	0.16	F814W	>24.69	>-7.27		1, 2
SN 2002hh	29.4	1.36	i	>23.19	>-9.51		1, 2, 3, 4
SN 2003gd (M3)	29.8	0.14	F814W	$24.44 \pm 0.04$	$-5.96 \pm 0.04$	yes	1, 5
SN 2004A	31.5	0.21	F814W	$24.8 \pm 0.12$	$-7.47 \pm 0.12$	yes	1, 5, 6
SN 2004dg	31.5	0.24	F814W	>25.44	>-6.86	•••	1
SN 2004et	29.4	0.42	$I_J$	$22.55 \pm 0.12$	$-7.73 \pm 0.12$	yes	1, 2, 4, 7
SN 2005cs	29.6	0.16	F814W	$24.06 \pm 0.07$	$-6.22 \pm 0.07$	yes	1, 5
SN 2006bc	30.8	0.21	F814W	>24.89	>-6.68	•••	1
SN 2006my	31.7	0.49	F814W	$25.3 \pm 0.13$	$-7.64 \pm 0.13$	yes	1, 5, 7
SN 2006ov	30.5	0.08	F814W	>24.64	>-6.38	• • • • • • • • • • • • • • • • • • • •	1, 7
SN 2007aa	31.6	0.03	F814W	>24.88	>-7.12		1
SN 2008bk	28.0	0.08	K	$20.19 \pm 0.03$	$-7.01 \pm 0.03$	yes	1, 2, 5, 8
SN 2008cn	32.6	0.33	F814W	$25.57 \pm 0.09$	$-7.97 \pm 0.09$	no	1, 9
SN 2012A	30.0	0.03	K	$22.09 \pm 0.13$	$-7.09 \pm 0.13$	yes	1, 10
SN 2012aw	30.0	0.43	K	$21.36 \pm 0.29$	$-7.97 \pm 0.29$	yes	1, 11
SN 2012ec	31.2	0.22	F814W	$23.83 \pm 0.08$	$-8.11 \pm 0.08$	no	1
SN 2013ej (M2)	29.8	0.14	F814W	$23.09 \pm 0.05$	$-7.07 \pm 0.05$	yes <sup>a</sup>	1, 10
SN 2017eaw	29.4	0.3	F606W	$26.48 \pm 0.05$	$-6.03 \pm 0.05$	no	4, 12
SN 2018zd	30.6	0.08	F814W	$25.13 \pm 0.15$	$-7.96 \pm 0.15$	yes	10, 13
SN 2018aoq	31.3	0.03	F814W	$24.35 \pm 0.02$	$-7.39 \pm 0.02$	no	4
SN 2018ivc	30.0	0.5	F606W	>25.48	>-8.13		14
SN 2019mhm	31.8	0.18	F814W	>24.53	>-8.01		15
SN 2020fqv	31.2	0.52	F606W	>24.8	>-10.04		16
SN 2020jfo	30.8	0.02	F814W	$25.46\pm0.07$	$-5.77 \pm 0.07$	no	17

**Notes.** All magnitudes are in the AB system. We adopt an M3 spectrum for SN 2003gd, an M2 spectrum for SN 201ej, and an M4 spectrum for all other RSGs. <sup>a</sup> Van Dyk et al. (2023) find that the flux at the position of SN 2013ej has faded below the pre-SN level in the F814W band, but the SN itself and a background source are detected in late-time images. The progenitor luminosity is therefore uncertain.

**References.** (1) Davies & Beasor (2018); (2) Smartt et al. (2009); (3) Kochanek (2020); (4) Davies & Beasor (2020); (5) Maund et al. (2014); (6) Maund (2017); (7) Crockett et al. (2011); (8) Van Dyk (2013); (9) Maund et al. (2015b); (10) Van Dyk et al. (2023); (11) Fraser (2016); (12) Van Dyk et al. (2019); (13) Hiramatsu et al. (2021); (14) Bostroem et al. (2020); (15) Vazquez et al. (2023); (16) Tinyanont et al. (2022); and (17) Sollerman et al. (2021).

 Table 8

 Detections of Partially Stripped Progenitor Stars from the Literature

SN	Type	Dist. Mod. (mag)	E(B-V) (mag)	Band	Mag (mag)	Bol. Mag (mag)	Faded?	References
SN 1987A	BSG	18.5	0.16	$V_{\rm i}$	$12.36 \pm 0.1$	$-5.91 \pm 0.1$	yes	1
SN 1993J	YSG	27.8	0.05	$R_{\rm c}^{'}$	$20.05 \pm 0.11$	$-7.75 \pm 0.11$	yes	2, 3
SN 2008ax	YSG	29.4	0.3	F606W	$23.94 \pm 0.42$	$-5.54 \pm 0.42$	yes	4, 5
SN 2011dh	YSG	29.5	0.07	F814W	$21.64 \pm 0.03$	$-7.91 \pm 0.03$	yes	5, 6, 7
SN 2013df	YSG	31.1	0.09	F555W	$24.51 \pm 0.07$	$-6.51 \pm 0.07$	no	5, 8
SN 2016gkg	YSG	32.1	0.09	F606W	$24.4 \pm 0.18$	$-7.67 \pm 0.18$	yes	9, 10
iPTF13bvn	SN Ib	31.8	0.045	F814W	$25.88 \pm 0.24$	$-5.39 \pm 0.24$	yes	11
SN 2019yvr	SN Ib	30.8	0.51	F635W	$24.90 \pm 0.02$	$-6.09 \pm 0.02$	no	12
SN 2017ein	SN Ic	31.4	0.41	F555W	$24.78 \pm 0.11$	$-6.73 \pm 0.11$	no	13

Notes. Original progenitor detections and their bolometric magnitudes, similar to Table 7.

**References.** (1) Walborn et al. (1989); (2) Aldering et al. (1994); (3) Maund et al. (2004); (4) Folatelli et al. (2015); (5) Smartt (2015); (6) Maund et al. (2015a); (7) Maund (2019); (8) Van Dyk et al. (2014); (9) Kilpatrick et al. (2022); (10) Van Dyk et al. (2023); (11) Eldridge & Maund (2016); (12) Kilpatrick et al. (2021); and (13) Xiang et al. (2019).

#### **ORCID iDs**

```
References
Abell, P. A., Allison, J., Anderson, S. F., et al. 2009, arXiv:0912.0201
Aldering, G., Humphreys, R. M., & Richmond, M. 1994, AJ, 107, 662
Basinger, C. M., Kochanek, C. S., Adams, S. M., Dai, X., & Stanek, K. Z.
   2021, MNRAS, 508, 1156
Bellm, E. C., Kulkarni, S. R., Graham, M. J., et al. 2019, PASP, 131, 018002
Blagorodnova, N., Neill, J. D., Walters, R., et al. 2018, PASP, 130, 035003
Bostroem, K. A., Valenti, S., Sand, D. J., et al. 2020, ApJ, 895, 31
Bruch, R. J., Gal-Yam, A., Schulze, S., et al. 2021, ApJ, 912, 46
Bruch, R. J., Gal-Yam, A., Yaron, O., et al. 2023, ApJ, 952, 119
Crockett, R. M., Smartt, S. J., Pastorello, A., et al. 2011, MNRAS, 410, 2767
Dálya, G., Díaz, R., Bouchet, F. R., et al. 2022, MNRAS, 514, 1403
Davies, B., & Beasor, E. R. 2018, MNRAS, 474, 2116
Davies, B., & Beasor, E. R. 2020, MNRAS, 493, 468
Davies, B., Plez, B., & Petrault, M. 2022, MNRAS, 517, 1483
Dekany, R., Smith, R. M., Riddle, R., et al. 2020, PASP, 132, 038001
Dressel, L., & Marinelli, M. 2023, Wide Field Camera 3 Instrument Handbook,
   Version 15.0 (Baltimore: STScI)
Efron, B. 1982, The Jackknife, the Bootstrap and other Resampling Plans
Eldridge, J. J., & Maund, J. R. 2016, MNRAS, 461, L117
Elias-Rosa, N., Van Dyk, S. D., Li, W., et al. 2011, ApJ, 742, 6
Ergon, M., Jerkstrand, A., Sollerman, J., et al. 2015, A&A, 580, A142
Folatelli, G., Bersten, M. C., Kuncarayakti, H., et al. 2015, ApJ, 811, 147
Förster, F., Moriya, T. J., Maureira, J. C., et al. 2018, NatAs, 2, 808
Fraser, M. 2016, MNRAS, 456, L16
Fremling, C., Miller, A. A., Sharma, Y., et al. 2020, ApJ, 895, 32
Gagliano, A., Izzo, L., Kilpatrick, C. D., et al. 2022, ApJ, 924, 55
Gal-Yam, A., Leonard, D. C., Fox, D. B., et al. 2007, ApJ, 656, 372
Graham, M. J., Kulkarni, S. R., Bellm, E. C., et al. 2019, PASP, 131, 078001
Hiramatsu, D., Howell, D. A., Van Dyk, S. D., et al. 2021, NatAs, 5, 903
Ho, A. Y. Q., Goldstein, D. A., Schulze, S., et al. 2019, ApJ, 887, 169
IRSA 2022, Zwicky Transient Facility Image Service, IPAC, doi:10.26131/
  IRSA539
Ivezić, Ž., Kahn, S. M., Tyson, J. A., et al. 2019, ApJ, 873, 111
Jacobson-Galán, W. V., Dessart, L., Jones, D. O., et al. 2022a, ApJ, 924, 15
Jacobson-Galán, W. V., Margutti, R., Kilpatrick, C. D., et al. 2020, ApJ,
Jacobson-Galán, W. V., Venkatraman, P., Margutti, R., et al. 2022b, ApJ,
   932, 58
Khazov, D., Yaron, O., Gal-Yam, A., et al. 2016, ApJ, 818, 3
Kilpatrick, C. D., Coulter, D. A., Foley, R. J., et al. 2022, ApJ, 936, 111
Kilpatrick, C. D., Drout, M. R., Auchettl, K., et al. 2021, MNRAS, 504, 2073
Kim, Y. L., Rigault, M., Neill, J. D., et al. 2022, PASP, 134, 024505
Kleiser, I. K. W., Poznanski, D., Kasen, D., et al. 2011, MNRAS, 415, 372
Kochanek, C. S. 2020, MNRAS, 493, 4945
Kochanek, C. S., Beacom, J. F., Kistler, M. D., et al. 2008, ApJ, 684, 1336
Kochanek, C. S., Khan, R., & Dai, X. 2012, ApJ, 759, 20
Kozyreva, A., Janka, H.-T., Kresse, D., Taubenberger, S., & Baklanov, P.
   2022, MNRAS, 514, 4173
```

```
Lançon, A., Gonneau, A., Verro, K., et al. 2021, A&A, 649, A97
Li, W., Leaman, J., Chornock, R., et al. 2011, MNRAS, 412, 1441
Li, W., Van Dyk, S. D., Filippenko, A. V., et al. 2006, ApJ, 641, 1060
Lupton, R. H., Gunn, J. E., & Szalay, A. S. 1999, AJ, 118, 1406
Margutti, R., Kamble, A., Milisavljevic, D., et al. 2017, ApJ, 835, 140
Masci, F. J., Laher, R. R., Rusholme, B., et al. 2019, PASP, 131, 018003
Maund, J. R. 2017, MNRAS, 469, 2202
Maund, J. R. 2019, ApJ, 883, 86
Maund, J. R., Arcavi, I., Ergon, M., et al. 2015a, MNRAS, 454, 2580
Maund, J. R., Fraser, M., Reilly, E., Ergon, M., & Mattila, S. 2015b, MNRAS,
Maund, J. R., Reilly, E., & Mattila, S. 2014, MNRAS, 438, 938
Maund, J. R., & Smartt, S. J. 2009, Sci, 324, 486
Maund, J. R., Smartt, S. J., Kudritzki, R. P., Podsiadlowski, P., &
   Gilmore, G. F. 2004, Natur, 427, 129
Morozova, V., Piro, A. L., Fuller, J., & Van Dyk, S. D. 2020, ApJL,
  891, L32
Neustadt, J. M. M., Kochanek, C. S., Stanek, K. Z., et al. 2021, MNRAS,
   508, 516
Ofek, E. O., & Ben-Ami, S. 2020, PASP, 132, 125004
Ofek, E. O., Sullivan, M., Shaviv, N. J., et al. 2014, ApJ, 789, 104
Pastorello, A., Smartt, S. J., Mattila, S., et al. 2007, Natur, 447, 829
Patterson, M. T., Bellm, E. C., Rusholme, B., et al. 2019, PASP, 131,
  018001
Patton, R. A., & Sukhbold, T. 2020, MNRAS, 499, 2803
Perley, D. A., Fremling, C., Sollerman, J., et al. 2020, ApJ, 904, 35
Reynolds, T. M., Fraser, M., & Gilmore, G. 2015, MNRAS, 453, 2885
Rigault, M. 2018, ztfquery, a python tool to access ZTF data, v1.0, Zenodo,
   doi:10.5281/zenodo.1345222
Rigault, M., Neill, J. D., Blagorodnova, N., et al. 2019, A&A, 627, A115
Rizzo Smith, M., Kochanek, C. S., & Neustadt, J. M. M. 2023, MNRAS,
   523, 1474
Rodríguez, Ó. 2022, MNRAS, 515, 897
Rui, L., Wang, X., Mo, J., et al. 2019, MNRAS, 485, 1990
Seitenzahl, I. R., Timmes, F. X., & Magkotsios, G. 2014, ApJ, 792, 10
Singh, A., Sahu, D. K., Anupama, G. C., et al. 2019, ApJL, 882, L15
Smartt, S. J. 2015, PASA, 32, e016
Smartt, S. J., Eldridge, J. J., Crockett, R. M., & Maund, J. R. 2009, MNRAS,
   395, 1409
Smith, N. 2017, RSPTA, 375, 20160268
Sollerman, J., Fransson, C., Barbarino, C., et al. 2020, A&A, 643, A79
Sollerman, J., Yang, S., Schulze, S., et al. 2021, A&A, 655, A105
Strotjohann, N. L., Ofek, E. O., Gal-Yam, A., et al. 2015, ApJ, 811, 117
Strotjohann, N. L., Ofek, E. O., Gal-Yam, A., et al. 2021, ApJ, 907, 99
Sun, N.-C., Maund, J. R., Crowther, P. A., et al. 2022, MNRAS, 510, 3701
Szczygieł, D. M., Gerke, J. R., Kochanek, C. S., & Stanek, K. Z. 2012, ApJ,
   747, 23
Tinyanont, S., Ridden-Harper, R., Foley, R. J., et al. 2022, MNRAS,
   512, 2777
Tsuna, D., Takei, Y., & Shigeyama, T. 2023, ApJ, 945, 104
Valerin, G., Pumo, M. L., Pastorello, A., et al. 2022, MNRAS, 513, 4983
Van Dyk, S. D. 2013, AJ, 146, 24
Van Dyk, S. D. 2017, RSPTA, 375, 20160277
Van Dyk, S. D., de Graw, A., Baer-Way, R., et al. 2023, MNRAS, 519, 471
Van Dyk, S. D., Zheng, W., Fox, O. D., et al. 2014, AJ, 147, 37
Van Dyk, S. D., Zheng, W., Maund, J. R., et al. 2019, ApJ, 875, 136
Vazquez, J., Kilpatrick, C. D., Dimitriadis, G., et al. 2023, ApJ, 949, 75
Verro, K., Trager, S. C., Peletier, R. F., et al. 2022, A&A, 660, A34
Walborn, N. R., Prevot, M. L., Prevot, L., et al. 1989, A&A, 219, 229
Weil, K. E., Fesen, R. A., Patnaude, D. J., & Milisavljevic, D. 2020, ApJ,
   900, 11
Wu, S. C., & Fuller, J. 2022, ApJL, 940, L27
Xiang, D., Wang, X., Mo, J., et al. 2019, ApJ, 871, 176
Yang, S., Sollerman, J., Strotjohann, N. L., et al. 2021, A&A, 655, A90
Yao, Y., Miller, A. A., Kulkarni, S. R., et al. 2019, ApJ, 886, 152
Zackay, B., Ofek, E. O., & Gal-Yam, A. 2016, ApJ, 830, 27
```